

# Lattice Boltzmann study of mass transfer for two-dimensional Bretherton/Taylor bubble train flow

A. Kuzmin<sup>\*,a</sup>, M. Januszewski<sup>b</sup>, D. Eskin<sup>c</sup>, F. Mostowfi<sup>c</sup>, J.J. Derksen<sup>a</sup>

<sup>a</sup>*Chemical and Materials Engineering, University of Alberta  
7th Floor, ECERF, 9107 116 St, Edmonton, Alberta, T6G 2V4 Canada*

<sup>b</sup>*Institute of Physics, University of Silesia, 40-007 Katowice, Poland*

<sup>c</sup>*Schlumberger DBR Technology Center  
9450 17 Ave NW, Edmonton, Alberta, T6N 1M9 Canada*

---

## Abstract

This work presents a procedure for the determination of the volumetric mass transfer coefficient in the context of lattice Boltzmann simulations for the Bretherton/Taylor bubble train flow for capillary numbers  $0.1 < Ca < 1.0$ . We address the case where the hydrodynamic pattern changes from having a vortex in the slug ( $Ca < 0.7$ ) to not having it ( $Ca > 0.7$ ) [1]. In the latter case the bubble shape is asymmetric and cannot be approximated through flat surfaces and circular circumferences as is often done in the literature [2, 3]. When the vortex is present in the slug, the scalar concentration is well mixed and it is common to use periodic boundary conditions and the inlet/outlet-averaged concentration as the characteristic concentration. The latter is not valid for flows where the tracer is not well mixed, i.e.  $Ca > 0.7$ . We therefore examine various boundary conditions (periodic, open, open with more than

---

\*Corresponding author, Telephone: +1(438)824-3695

*Email addresses:* kuzmin@ualberta.ca (A. Kuzmin), michalj@gmail.com (M. Januszewski), deskin@slb.com (D. Eskin), fmostowfi@slb.com (F. Mostowfi), jos@ualberta.ca (J.J. Derksen)

1 unit cell) and definitions of the characteristic concentration to estimate mass transfer coefficients for the range of capillary numbers  $0.1 < Ca < 1.0$ . We show that the time-dependent volume averaged concentration taken as the characteristic concentration produces the most robust results and that all strategies presented in the literature are extreme limits of one unified equation. Finally, we show good agreement of simulation results for different Peclet numbers with analytical predictions of van Baten and Krishna [2].

*Key words:* Mass Transfer, Taylor/Bretherton bubble train flow, Multiphase flow, Lattice Boltzmann method, Binary liquid model, Flow in microchannels with parallel plates

---

## 1 1. Introduction

2 Monolith reactors have recently been getting more attention as a promis-  
3 ing alternative to slurry reactors and trickle bed reactors [3, 4]. These re-  
4 actors usually operate in the Bretherton-Taylor regime [5, 6] which is a flow  
5 of equally sized, long air bubbles through a liquid medium, see Fig. 1. This  
6 flow regime is characterized by the dominance of surface tension over inertia  
7 and viscous effects, and by comparatively small gas flow velocities [7]. Due to  
8 the dominance of surface tension, the flow exhibits advantageous properties  
9 which cannot be achieved in its macroscopic counterparts: thin liquid films  
10 [5] between bubbles and walls strongly enhance mass transfer from gas and  
11 walls to liquid; the plug flow regime occurring in monolith reactors allows to  
12 perform chemical reactions in slugs only [3]. Moreover, the low slip velocity  
13 between gas and liquid is utilized in experiments to measure liquid velocity  
14 [6]: bubbles travelling with approximately the same velocity as liquid can be

15 captured with a camera. These properties explain why nowadays one can find  
 16 a large number of applications of the Bretherton-Taylor bubble train flow:  
 17 continuous flow analyzers to measure liquid velocity, chemical reactors for  
 18 hydrogenation of nitroaromatics, 2-ethyl-hexenal, Fischer-Tropsch synthesis,  
 19 etc. The extensive reviews of Kreutzer et al. [3], Gupta et al. [8], Yue et al.  
 20 [7] cover a significant number of applications.

This work is focused on gas to liquid mass transfer for the two-dimensional Bretherton/Taylor flow. A good understanding of mass transfer and how it depends on parameters such as the capillary number, the Reynolds number, and slug and bubble lengths allows to properly manufacture a microchannel with properties necessary to ensure that chemical reactions are performed in the best possible manner. The mass transfer coefficient is defined as the flux from the gas-liquid interface divided by the difference of the imposed concentration and the characteristic concentration in the domain. The concentration distribution in the domain is prescribed by underlying hydrodynamics fields. For example, experimental studies [7, 4] show a complex dependency of the mass transfer coefficient on flow parameters: bubble and slug lengths, and bubble velocity, which in turn relate to the capillary number  $Ca$  and the Reynolds number  $Re$ . Yue et al. [7] established an experimental correlation for the volumetric mass transfer coefficient for a bubble train as a function of the diffusion coefficient, slug and bubble lengths, and bubble velocity:

$$k_L a = \frac{2}{d_h} \left( \frac{DU_{\text{bubble}}}{L_{\text{bubble}} + L_{\text{slug}}} \right)^{0.5} \left( \frac{L_{\text{bubble}}}{L_{\text{bubble}} + L_{\text{slug}}} \right)^{0.3}, \quad (1)$$

21 where  $k_L a$  is the volumetric mass transfer coefficient,  $d_h$  is the hydraulic  
 22 diameter,  $L_{\text{bubble}}$  is the bubble length,  $L_{\text{slug}}$  is the slug distance (between  
 23 bubbles),  $U_{\text{bubble}}$  is the bubble velocity, and  $D$  is the diffusion coefficient.

The understanding of mass transfer for the bubble train flow is not possible without knowledge of hydrodynamic patterns. There are several works studying the hydrodynamic properties of the bubble train flow, both experimental [9, 10, 11] and numerical [12, 13, 1, 14, 15]. For the flow of long bubbles between parallel plates chosen here as the study case, it is indicated that there exists a vortex in the liquid slug for  $Ca < 0.7$ , and that the bubble shape is symmetric for low capillary numbers ( $Ca < 0.1$  [11]) with the capillary number defined as:

$$Ca = \frac{\mu_{\text{liq}} U_{\text{bubble}}}{\gamma}, \quad (2)$$

where  $\mu_{\text{liq}}$  is the liquid viscosity,  $U_{\text{bubble}}$  is the bubble velocity, and  $\gamma$  is the interfacial tension. The fact that the bubble shape for  $Ca < 0.1$  can be represented as two hemicircles and two planar interfaces with the vortex existing in the liquid slug has been utilized for analytical estimations of mass transfer properties.

Since the mass transfer coefficient is defined in terms of a mass flux through a certain area, see Sec 2, analytical estimates [3, 16] are based on a decomposition of the bubble surface in parts. The mass transfer coefficient is calculated through two separate contributions from two planar films and two hemicircles. For both contributions the Higbie penetration theory [17] is utilized, which states that the mass transfer coefficient for a simple flow geometry depends on the average time a liquid packet interacts with a geometrical feature. It can be calculated as  $\sqrt{\frac{\pi D}{t_{\text{char}}}}$ , where  $t_{\text{char}}$  is the interaction time. As an example of the application of the Higbie penetration theory, the mass transfer coefficient for the flow of bubbles between parallel plates

is calculated as (similar to the work of van Baten and Krishna [2]):

$$k_L = 2\sqrt{\frac{\pi D}{t_{\text{film}}}} + 2\sqrt{\frac{\pi D}{t_{\text{circle}}}}, \quad (3)$$

where  $t_{\text{film}} = \frac{L_{\text{film}}}{U_{\text{bubble}}}$  stands for the interaction time of liquid traveling next to the planar part of the bubble, and  $t_{\text{circle}} = \frac{\pi R_{\text{circle}}}{U_{\text{bubble}}}$  is the time during which the liquid in the slug travels the distance of half the bubble cap circumference.

Despite their simplicity, such analytical expressions work well for flows with low capillary numbers  $Ca < 0.1$  [4] where the bubble shape is symmetrical and can be approximated with good precision. Moreover, because of the hydrodynamic pattern in the slug (i.e. presence of a vortex in the slug), one can estimate the time for a fluid batch to travel the whole circumference. However, with the increase of the capillary number the situation changes significantly – the symmetrical bubble shape is lost and the bubble resembles a bullet [18]. For flows with  $Ca > 0.7$  there is also no vortex in the liquid slug. In this case the Higbie theory fails to estimate the contribution from bubble caps, which explains the need to turn to numerical simulations where all hydrodynamic fields as well as complex bubble shapes are taken into account.

Typical numerical studies of mass transfer [3, 2] do not consider the simulation of bubble shapes for  $Ca > 0.1$ . The interesting work by Onea et al. [19] only takes into account short length bubbles in microchannels with a square cross section. As well, in this work a Schmidt number of around 0.8 is used: thus, the thickness of the concentration and momentum boundary layer is similar leading to qualitative results since it's not possible to separate mixing due to hydrodynamics patterns from mixing due to diffusion.

The usual simulation of mass transfer is performed as follows:

52 **I** The bubble shape is calculated either through analytical correlations [5] or  
 53 experimental correlations [11] without directly resolving bubble shapes  
 54 through multiphase simulations. The expressions for bubble shapes are  
 55 available only for flows with capillary number  $Ca < 0.1$ .

56 **II** Hydrodynamic fields are then obtained by performing simulations of one-  
 57 component flow around the bubble by imposing the bubble velocity on  
 58 the channel walls. Thus, the simulations are performed in the reference  
 59 frame moving with the bubble. A stress-free condition is imposed at  
 60 the bubble surface.

**III** The mass transfer simulations are performed in the reference frame mov-  
 ing with the bubble. The saturation concentration is imposed at the  
 bubble surface. Only one unit cell containing a single bubble is used for  
 simulations. Periodic concentration boundary conditions are utilized to  
 determine the volumetric mass transfer coefficient, which is calculated  
 through the following equation [2]:

$$k_L a = \frac{\overline{\text{Flux}}}{C_{\text{bubble}} - \langle C_{\text{in/outlet}} \rangle} \frac{\text{bubble surface area}}{\text{unit cell volume}}, \quad (4)$$

61 where  $\langle C_{\text{in/outlet}}(t) \rangle = \int C U_{\text{in/outlet}} dA / \int U_{\text{in/outlet}} dA$  is the space-averaged  
 62 inlet/outlet (periodic boundary conditions) concentration as a function  
 63 of time. Therefore, in terms of the mass transfer definition,  $\langle C_{\text{in/outlet}}(t) \rangle$   
 64 plays the role of the characteristic concentration. The time-averaged  
 65 concentration flux ( $\overline{\text{Flux}}$ ) is calculated as the difference between the  
 66 overall average concentration in the whole domain ( $\langle C_{\text{overall}} \rangle = \int_V C dV / V$ )  
 67 at time  $t_1$  and at time  $t_2$  divided by the time difference  $t_2 - t_1$ . The

68 agreement between numerical simulations [2] and experimental corre-  
69 lations of Bercic and Pintar [4] was good.

70 The presented numerical approaches [2, 3] can be criticized on a number of  
71 points. They mainly relate to the bubble shape approximation, which is taken  
72 to be symmetrical, i.e. consisting of two hemispheres and film for the case  
73 of flow in circular capillaries. This is valid for small capillary numbers only  
74 ( $Ca < 0.1$ ). As previously discussed, for such capillary numbers the tracer  
75 is well mixed in the slug and the choice of the characteristic concentration  
76 needed for the mass transfer coefficient, Eq. 5, is obvious. With minimal  
77 differences in the results, it can either be the averaged concentration in the  
78 liquid slug or the inlet/outlet space-averaged concentration. The latter is  
79 used in the formulation of van Baten and Krishna [2] presented above.

80 While it is clear that periodic boundary conditions can be employed for  
81 the calculation of hydrodynamic fields, the same does not apply to the mass  
82 transfer coefficient simulations. Experimental correlations [4] show that the  
83 concentration in a bubble train along the streamwise direction changes ex-  
84 ponentially with distance. Mass transfer simulations however, are made only  
85 for one unit cell using periodic boundary conditions with the same concen-  
86 tration at the inlet and at the outlet. The question how a single unit cell  
87 simulation corresponds to experimental measurements arises where the con-  
88 centration difference is measured at distances of at least a few unit cells [4].  
89 In other words, one needs to understand how the discrete one unit cell simu-  
90 lation corresponds to the continuous picture in experiments where one does  
91 not distinguish discrete bubbles but takes measurements of concentration at  
92 different locations.

Addressing situations for a rich number of hydrodynamic patterns, shapes, and effects of bubble lengths, etc for bubble train flows, we feel that there is a need to examine carefully the strategies and assumptions behind the numerical calculations of the mass transfer coefficient. We aim at establishing clear procedures as to how properly obtain the mass transfer coefficient via a study of different boundary conditions and different definitions of the characteristic concentration. The case we want to examine is a two-dimensional bubble train flow between parallel plates. We address the following:

**I** Applicability of periodic boundary conditions to determine the mass transfer coefficient when the vortex in the slug disappears, i.e. when  $Ca > 0.7$ .

**II** Validity of the inlet/outlet-averaged or domain-averaged concentrations as characteristic concentrations in the definition of the mass transfer coefficient.

**III** Translation of the continuous experimental picture to numerical simulations of a few unit cells, the issue of correspondence between space averages (simulations [2]) and time averages (experiment).

In addition, at the end of the manuscript we present results of the dependence of the volumetric mass transfer coefficient on the Peclet number that we compare with analytical [16] and experimental correlations [7]. The thorough determination of the mass transfer coefficient and associated Sherwood number as a function of other non-dimensional parameters such as gas holdup, bubble/slug lengths, and the capillary number is left for future studies.



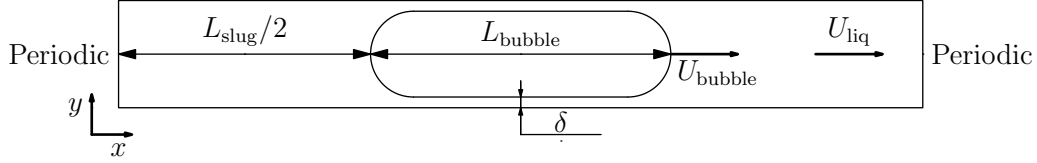


Figure 1: Simplified sketch of the bubble motion. Using periodic conditions for the velocity field is natural, but needs evaluation for mass transfer.

116 To establish numerical procedures we performed multiphase simulations  
 117 to extract bubble shapes [18, 13] for the range of capillary numbers  $Ca =$   
 118  $0.1 - 1.0$ . For this range of capillary numbers we were able to capture the  
 119 bubble shape change and the change of hydrodynamic patterns. The mass  
 120 transfer simulations presented here were performed with various boundary  
 121 conditions (open, periodic) and with a few unit cells (1 to 10 unit cells). As  
 122 our numerical approach we take the lattice Boltzmann method, a relatively  
 123 new CFD competitor developed during the last 20 years [20, 21, 22, 23]. This  
 124 method was successfully applied to simulate not only single phase hydrody-  
 125 namic problems [24], but also multiphase flows [25, 26, 27], heat transfer  
 126 [28, 29], and ferrofluids [30, 31].

127 Mass transfer problems in the lattice Boltzmann framework were mainly  
 128 addressed in a series of works of Ginzburg and co-authors [32, 33, 34]. In con-  
 129 trast to these works whose focus was on simulating the advection-diffusion  
 130 equation via the lattice Boltzmann framework, we concentrate on the ap-  
 131 plication side. One should also mention the work of Yoshino and Inamuro  
 132 [35] about heat and mass transfers in porous media and the work of Derksen  
 133 [36] simulating lateral mixing in cross-channel flow. The last two works are  
 134 focused on problems of homogeneous nature and do not provide guidance as

135 to how to obtain the mass transfer coefficient for heterogeneous cases.

136 The paper is organized as follows. We start with definitions of the volu-  
137 metric mass transfer coefficient and apply them to bubble train flow in order  
138 to derive expressions to connect space- and time-averages. Then, the lattice  
139 Boltzmann model used to simulate mass transfer is presented, followed by  
140 benchmarks. Finally, numerical simulations of various boundary conditions  
141 and simulations spanning a few unit cells for different hydrodynamic pat-  
142 terns are presented to establish the procedure to determine the volumetric  
143 mass transfer coefficient. The comparison with analytical correlations is also  
144 discussed.

## 145 2. Mass transfer definitions

By definition, the mass transfer coefficient from a surface with an imposed  
constant concentration  $C_{\text{bubble}}$  is:

$$k_L = \frac{\dot{m}}{P\Delta C}, \quad \Delta C = C_{\text{bubble}} - C_{\text{medium}}, \quad (5)$$

146 where  $\dot{m}$  is the mass flux  $\left[\frac{kg}{s}\right]$ ,  $P$  is the area of the surface  $\left[m^2\right]$ , and  $\Delta C$  is  
147 the concentration difference between the surface and the surrounding medium  
148  $\left[\frac{kg}{m^3}\right]$ . Therefore,  $k_L$  has units of  $\left[\frac{m}{s}\right]$ . Usually, the surrounding medium  
149 concentration is taken at an infinite distance from the bubble. However, in  
150 the case of complicated geometries and non-homogeneous concentrations, the  
151 medium concentration can be the average concentration in the domain or the  
152 flux-averaged concentration at the inlet or outlet, etc. Thus, one needs to  
153 establish a clear definition of  $\Delta C$  to determine the volumetric mass transfer  
154 coefficient in the case of complex geometries and non-trivial hydrodynamic  
155 velocity patterns.

156 We first examine the definitions of mass transfer in the case of point  
157 sources.

### 158 2.1. Point mass sources

159 In what follows we will present three approaches to calculate point mass  
160 transfer coefficients (by point source we assume the source to have an in-  
161 finitesimally small surface area  $P$ ):

1. Let us look at the infinitesimally small domain of volume  $A\Delta x$ , not moving and containing a point source. The concentration difference is  $\Delta C = C^* - C(t)$ , where  $C^*$  is the imposed point source concentration, and  $C(t)$  is the time-dependent concentration, which does not depend on the location due to the assumption of homogeneity. One can therefore write a time-dependent ordinary differential equation for the concentration in the domain:

$$\dot{m} = A\Delta x \frac{dC}{dt} = k_L P (C^* - C(t)), \quad (6)$$

with the initial condition  $C(0) = 0$ . The solution can be found as:

$$C(t) = C^* (1 - \exp(-k_L a t)), \quad (7)$$

where  $k_L a$  is the volumetric mass transfer coefficient defined as:

$$k_L a = k_L \frac{P}{A\Delta x} = k_L \frac{P}{V}, \quad (8)$$

162 where  $P$  is the source surface,  $V$  is the unit cell volume.

- 163 2. Let us predict mass transfer in a liquid moving with the velocity  $U$ , see  
164 Fig. 2.

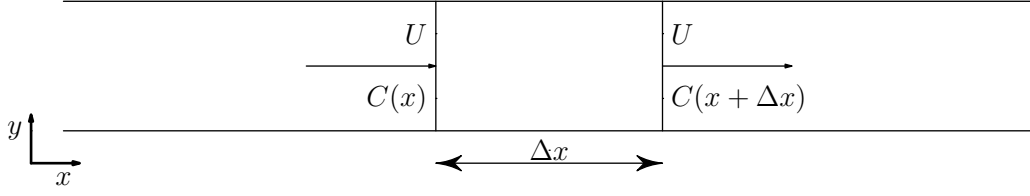


Figure 2: The mass transfer in a moving liquid.

If one can assume that the point mass sources are homogeneously distributed in the whole medium, the mass accumulated in the volume  $V = A\Delta x$  can be calculated as the difference of mass fluxes entering and leaving the domain  $U(C(x + \Delta x) - C(x))$ . The accumulated mass should be proportional to the mass transfer coefficient:

$$U(C(x + \Delta x) - C(x)) = k_L P(C^* - C(x)), \quad (9)$$

giving the same solution, now in the spatial domain:

$$C(x) = C^* \left( 1 - \exp\left(-k_L a \frac{x}{U}\right) \right). \quad (10)$$

165 Note that the concentration  $C(x)$  does not depend on time.

166 3. If one transfers to the frame moving with the liquid velocity  $U$ , the  
 167 situation will be the same as in the first case. One can connect time  
 168 and space with the velocity  $U$  ( $t = \frac{x}{U}$ ).

## 169 2.2. Bubble train

170 In the application to bubble train flow it is useful to think of one bubble  
 171 as a point source to be able to use the calculations presented above. For  
 172 example, the expression (10) was used in experiments by Bercic and Pintar  
 173 [4]. However, one should be accurate with the definition of velocities because

174 two different phases co-exist in the bubble train flow. Usually, one can take  
175 the velocity  $U$  to be a bulk velocity or  $U = U_{\text{gas}} + U_{\text{liq}}$ , where  $U_{\text{gas}}$  and  
176  $U_{\text{liq}}$  are liquid and gas superficial velocities, respectively. The gas and liquid  
177 superficial and actual velocities are connected with each other through a  
178 complex dependency on  $Ca$ ,  $\epsilon$  [13].

179 With experimental measurements of concentration at different locations,  
180 the calculation of the mass transfer coefficient using the logarithmic func-  
181 tion is straightforward. However, if one wants to analytically or numerically  
182 calculate the mass transfer coefficients, the situation is much more compli-  
183 cated because of the presence of two phases and complex bubble geometry.  
184 As was mentioned before, depending on the capillary number the velocity  
185 pattern and thus scalar mixing is different. Analytical approaches [16, 2]  
186 assume that the contributions from film and bubble caps can be calculated  
187 separately. Therefore, tracer from the film does not influence bubble caps  
188 diffusion. However, this assumption overpredicts mass transfer for a number  
189 of experiments [16]. This happens since some tracer concentration from the  
190 film is mixed with the slug and increases the overall concentration in the  
191 slug, thereby decreasing the mass transfer from the bubble caps. Therefore,  
192 the analytical estimates for the mass transfer coefficient calculation do not  
193 account for mutual mass transfer from neighbouring bubbles.

194 Overall, mixing patterns of the film and liquid slugs are of great im-  
195 portance for the estimation of mass transfer [7]. However, the assumptions  
196 usually taken for mass transfer calculations are small capillary numbers and  
197 certain mixing patterns such as to help to estimate the mass transfer using  
198 the penetration theory of Higbie [17].

199 In comparison with analytical calculations and simplifications, the nu-  
 200 merical approach can take into account the complex mixing patterns and  
 201 geometries. However, there are challenges as to how to mimic the continuous  
 202 picture where the medium is moving with bulk velocity  $U = U_{\text{gas}} + U_{\text{liq}}$  as  
 203 it is done in experiments. Thus, the questions indicated in Section 1 arise.  
 204 The next section gives more details about numerical simulations.

### 205 *2.3. Numerical simulations*

206 Ideally one wants to mimic the continuous picture as it is seen in ex-  
 207 periments. Thus, mass transfer simulations for a number of unit cells each  
 208 containing a bubble are needed. As was indicated above, there are two ap-  
 209 proaches towards it – either to simulate the bubble train and then to measure  
 210 concentration along the pipe, Eq. 10, or to transfer to the reference frame  
 211 moving with the bulk velocity  $U$  and conduct the same measurements. How-  
 212 ever, both methods require tracking of moving bubbles which is complicated  
 213 from the numerical point of view. Therefore, one needs to come up with a  
 214 simple and smaller domain for calculations of the mass transfer coefficient,  
 215 which closely mimics the continuous picture of a large number of separated  
 216 bubbles.

217 To avoid complications with moving grids, our approach is to simulate  
 218 mass transfer in a reference frame moving with the bubble. Therefore, one  
 219 needs to examine Eq. 10 more closely.

We perform simulations in the frame co-moving with the bubble in which  
 the bubble position stays constant. The bubble velocity  $U_{\text{bubble}}$  is different  
 from the bulk velocity  $U = U_{\text{gas}} + U_{\text{liq}}$ , and one thus needs to perform a  $x$

coordinate variable change:

$$\begin{aligned}
x(t) &= U_{\text{bubble}} t \\
\overline{C(x)} &= C^* \left( 1 - \exp\left(-k_L a \frac{x}{U_{\text{gas}} + U_{\text{liq}}}\right) \right) \\
\langle C(t) \rangle &= C^* \left( 1 - \exp\left(-k_L a t \frac{U_{\text{bubble}}}{U_{\text{gas}} + U_{\text{liq}}}\right) \right),
\end{aligned} \tag{11}$$

where  $\langle C(t) \rangle$  is the space-averaged characteristic concentration, and  $\overline{C(x)}$  is the time-averaged concentration at location  $x$ . One can make different choices for  $\langle C(t) \rangle$  such as the concentration averaged over the whole domain or inlet/outlet space-averaged concentrations as used in [2, 3]. The volumetric mass transfer coefficient can be obtained through the space-averaged concentration:

$$\begin{aligned}
k_L a t \frac{U_{\text{bubble}}}{U_{\text{gas}} + U_{\text{liq}}} &= \ln \frac{C^*}{C^* - \langle C(t) \rangle} \\
k_L a \frac{L_{\text{unit}}}{U_{\text{liq}} + U_{\text{gas}}} &= \frac{L_{\text{unit}}}{U_{\text{bubble}} t} \ln \frac{C^*}{C^* - \langle C(t) \rangle},
\end{aligned} \tag{12}$$

where the parameter  $k_L a \frac{L_{\text{unit}}}{U_{\text{gas}} + U_{\text{liq}}}$  is non-dimensional. One can also measure the volumetric mass transfer coefficient from concentrations given at times  $t_1$  and  $t_2$ :

$$k_L a \frac{L_{\text{unit}}}{U_{\text{liq}} + U_{\text{gas}}} = \frac{L_{\text{unit}}}{U_{\text{bubble}}(t_2 - t_1)} \ln \frac{C^* - \langle C(t_1) \rangle}{C^* - \langle C(t_2) \rangle}. \tag{13}$$

220 Expressions (11 - 13) are the cornerstones of the present work . Four possible  
221 scenarios of numerical simulations have been examined:

- 222 1. One unit cell is simulated with periodic boundary conditions, see Fig.
- 223 3. In this case no tracer leaves the domain similarly to plug flow.
- 224 Though easier to implement, it gives rise to the criticism that the inlet

225 concentration is equal to the outlet one. As was discussed, in exper-  
 226 iments there is a concentration difference between the inlet and the  
 227 outlet, even for one unit cell.

In this case, the volumetric mass transfer coefficient is calculated by Eq. 12. The characteristic concentration  $\langle C(t) \rangle$  required for the volumetric mass transfer coefficient is taken as the average concentration in the domain:

$$C(t) = \frac{\int_{liquid} C dV}{\int dV}. \quad (14)$$

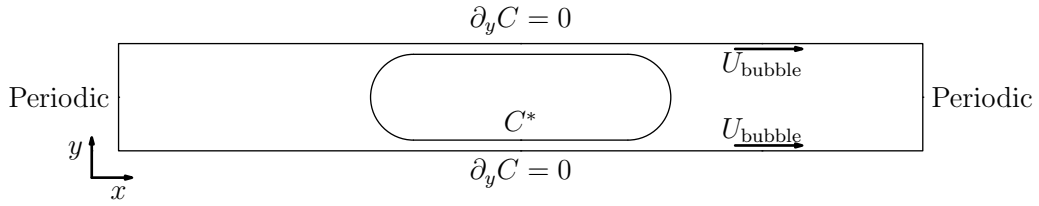


Figure 3: The two-dimensional benchmark for the the mass transfer coefficient for the bubble located at the middle of the domain.

228

2. Periodic boundary conditions are applied as in the first case but the characteristic concentration is taken as the inlet/outlet flux-averaged concentration [2]:

$$\begin{aligned} \langle C_{\text{inlet}}(t) \rangle &= \frac{\int U(y)C(0, y, t)dy}{\int U(0, y)dy} \\ \langle C_{\text{outlet}}(t) \rangle &= \frac{\int U(y)C(L_{\text{unit}}, y, t)dy}{\int U(L_{\text{unit}}, y)dy} \\ C_{\text{inlet}}(\mathbf{x}, t) &= C_{\text{outlet}}(\mathbf{x}, t), \text{ due to periodicity.} \end{aligned} \quad (15)$$



229 The assumptions of this approach are that the concentration difference  
 230 between the inlet/outlet- and the space-averaged over the whole unit  
 231 cell is not significant. Thus, the tracer is assumed to be well mixed in  
 232 the slug.

3. The approach of van Baten and Krishna [2], where periodic boundary conditions are used and the mass transfer coefficient is calculated as the gain of the mass in the system divided by the concentration difference multiplied by the surface area:

$$k_L a = \frac{\dot{m}}{P \Delta C} \frac{P}{V} = \frac{\dot{m}}{V(C^* - \langle C(t) \rangle)}, \quad (16)$$

where the mass flux in the domain can be calculated as:

$$\dot{m} = \frac{m_2 - m_1}{t_2 - t_1} = \frac{\int_{liq} C(\mathbf{x}, t_2) d\mathbf{x} - \int_{liq} C(\mathbf{x}, t_1) d\mathbf{x}}{t_2 - t_1}. \quad (17)$$

233 In the approach of van Baten and Krishna the inlet/outlet flux-averaged  
 234 concentrations were taken as the characteristic concentration  $\langle C(t) \rangle$ .

- 235 4. Simulation of several unit cells, see Fig. 4. This situation corresponds  
 236 to the head of the bubble train, after injection in the pipe and travel-  
 237 ling along the channel. One can see that this situation best resembles  
 238 the experimental picture, but also requires larger computational re-  
 239 sources. By simulating a certain number of bubbles in the train head,  
 240 the influence of the boundaries can be reduced. For example, left and  
 241 right boundary conditions in this case are taken as open boundaries,  
 242 i.e.  $\partial C / \partial x = 0$ . There is no ambiguity in the choice of the characteris-  
 243 tic concentration. The average concentration of any unit cell far away  
 244 from boundaries will be governed by Eq. 13.

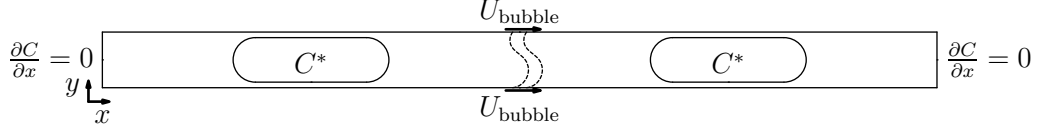


Figure 4: Benchmark for multiple unit cells.

One can notice that all examined cases are the extreme limits of one equation:

$$k_L a = \frac{\dot{m} - \int C_{\text{outlet}}(t)u(L_{\text{unit}}, y)dy + \int C_{\text{inlet}}(t)u(0, y)dy}{V\Delta C}, \quad (18)$$

where  $\Delta C = C^* - \langle C(t) \rangle$  with  $\langle C(t) \rangle$  taken to be the average concentration in the whole liquid domain,  $\dot{m}$  is the mass gain in the domain,  $\int C_{\text{inlet}}u(0, y)dy$  and  $\int C_{\text{outlet}}u(L_{\text{unit}}, y)dy$  are inlet/outlet mass fluxes. Eq. 18 describes the mass balance: whatever was generated by the bubble surface equals the domain mass change minus whatever left the domain plus whatever entered it.

With periodic boundary conditions:

$$\int C_{\text{outlet}}(t)u(L_{\text{unit}}, y)dy = \int C_{\text{inlet}}(t)u(0, y)dy.$$

In this case, Eq. 18 reduces to Eq. 16.

Another limiting case (will be shown later) is when the mass accumulation rate equals zero, i.e.  $\dot{m} = 0$ . This situation corresponds to a simulation of a few unit cells with open boundary for flows with  $Ca > 0.7$ .

Before we examine all the test cases above, some lattice Boltzmann mass transfer benchmarks will be presented.

### 257 3. Validation

258 As was discussed earlier, analytical correlations for the mass transfer co-  
 259 efficient have been derived for a Taylor bubble train flow as two separate  
 260 contributions: the mass transfer from two half circles and the mass transfer  
 261 from the film. We will examine these mass transfer cases closely with the  
 262 help of the lattice Boltzmann method and compare them against analyti-  
 263 cal solutions. The next sections will give a short introduction to the lattice  
 264 Boltzmann method and present benchmark results.

#### 265 3.1. TRT D2Q9 model

The lattice Boltzmann equation (LBE) operates on a square/cubic grid representing the physical domain in non-dimensional terms (hereafter we use subscript LB to denote non-dimensional quantities). It utilizes probability distribution functions (also known as particle populations) containing information about macroscopic variables, such as fluid density and momentum. The LBE consists of two parts: a local collision step, and a propagation step which transports information from one node to another along directions specified by a discrete velocity set. The LBE is typically implemented as follows:

$$\begin{aligned} f_i^*(\mathbf{x}, t) &= f_i(\mathbf{x}, t) - \omega(f_i(\mathbf{x}, t) - eq_i(\mathbf{x}, t)), & \text{collision step} \\ f_i(\mathbf{x} + \mathbf{c}_i, t + 1) &= f_i^*(\mathbf{x}, t), & \text{propagation step,} \end{aligned} \tag{19}$$

266 where  $f_i$  is the probability distribution function in the direction  $\mathbf{c}_i$ ,  $eq_i$  is  
 267 the equilibrium probability distribution function, and  $\omega$  is the relaxation  
 268 parameter. The term  $-\omega(f_i - eq_i)$  is the so-called BGK collision operator  
 269 [37]. However, the approach used here is the TRT (two-relaxation-times)

270 collision operator [32, 34]. In comparison with the widely used BGK collision  
 271 operator, the TRT collision operator has better accuracy for diffusion and  
 272 convection fluxes, as well as a larger range of parameters where the scheme  
 273 is stable.

The TRT collision operator [38] decomposes the populations and the equilibrium distribution into a symmetric and an antisymmetric part:

$$f_i^\pm = \frac{f_i \pm f_{\bar{i}}}{2}, \quad eq_i^\pm = \frac{eq_i \pm eq_{\bar{i}}}{2}, \quad (20)$$

where  $\bar{i}$  is the direction opposite to the  $i$ -th direction. The collision is performed with two independent relaxation rates for symmetric and antisymmetric modes:

$$\begin{aligned} f_i^*(\mathbf{x}, t) &= f_i(\mathbf{x}, t) - \omega_+(f_i^+ - eq_i^+) - \omega_-(f_i^- - eq_i^-) \\ f_i(\mathbf{x} + \mathbf{c}_i, t + 1) &= f_i^*(\mathbf{x}, t). \end{aligned} \quad (21)$$

274 Note that the TRT collision operator reduces to the BGK operator if  $\omega_+ =$   
 275  $\omega_-$ . In comparison with the BGK collision operator, the TRT collision operator  
 276 has one additional degree of freedom. The TRT operator introduces the  
 277 following free parameter  $\Lambda = \left(\frac{1}{\omega_+} - \frac{1}{2}\right)\left(\frac{1}{\omega_-} - \frac{1}{2}\right)$ . This free parameter controls  
 278 the effective location of bounce-back walls [39], second-order accuracy of the  
 279 boundary [38] and interface schemes [40], spatial accuracy [41, 42], consistency  
 280 [43] and, to some extent, stability [44, 45, 42]. In particular,  $\Lambda = \frac{1}{4}$   
 281 achieves the optimal stability for the isotropic advection-diffusion equation  
 282 [44].

The parameters  $\omega_+$ ,  $\omega_-$  and  $eq_i$  fully define the lattice Boltzmann procedure. The two-dimensional, nine-velocity LBM  $D2Q9$  we used in this work

is defined on the set of lattice velocities with components:

$$\begin{aligned} c_{ix} &= \{0, 1, 0, -1, 0, 1, -1, -1, 1\}, \text{ for } i = 0 \dots 8 \\ c_{iy} &= \{0, 0, 1, 0, -1, 1, 1, -1, -1\}, \text{ for } i = 0 \dots 8. \end{aligned} \quad (22)$$

The equilibrium functions for the  $D2Q9$  TRT model are represented as [44]:

$$\begin{aligned} eq_i^+ &= eq_i^{(m)} + g^{(u)} eq_i^{(u)} \\ eq_i^{(m)} &= t_i^{(m)} c_e + eq_i^{(a)} \\ eq_i^{(u)} &= t_i^{(u)} \frac{u_{LB,x}^2 + u_{LB,y}^2}{2} + \frac{u_{LB,x}^2 - u_{LB,y}^2}{4} p_i^{(xx)} + g_{xy}^{(u)} \frac{u_{LB,x} u_{LB,y}}{4} p_i^{xy} \\ eq_i^{(a)} &= \frac{K_{LB,xx} - K_{LB,yy}}{4} p_i^{xx} + \frac{K_{LB,xy}}{4} p_i^{(xy)} \\ eq_i^- &= t_i^{(a)} u_{LB,\alpha} c_{i\alpha}, \end{aligned} \quad (23)$$

where  $K_{LB,xx,yy,xy}$  are proportional to components of the diffusion tensor,  $c_e = \frac{K_{LB,xx} + K_{LB,yy}}{2}$ , parameters  $g^{(u)}$  and  $g_{xy}^u$  are either zero or one (see below), and the tensor  $p_i^{(xx)} = c_{ix}^2 - c_{iy}^2$ , the tensor  $p_i^{(xy)} = c_{ix} c_{iy}$ , the weights  $t_i^{(u,m,a)}$  can be chosen based on stability criteria. The most commonly used set of weights, the so-called “hydrodynamic” weights, were chosen:

$$t_i^{(u)} = t_i^{(m)} = t_i^{(a)} = \left\{ 0, \frac{1}{3}, \frac{1}{3}, \frac{1}{3}, \frac{1}{3}, \frac{1}{12}, \frac{1}{12}, \frac{1}{12}, \frac{1}{12} \right\} \quad (24)$$

It can be shown through the Chapman-Enskog procedure [46], that the simple update rule with the equilibrium function presented above restores the anisotropic advection-diffusion equation:

$$\partial_t C_{LB} + \partial_\alpha C_{LB} u_{LB,\alpha} = \partial_{\alpha\beta} D_{LB,\alpha\beta} C_{LB}, \quad (25)$$

where the concentration  $C_{LB} = \sum_i f_i$ , and  $D_{LB,\alpha\beta} = \left( \frac{1}{\omega_-} - \frac{1}{2} \right) K_{LB,\alpha\beta}$  is the

following diffusion tensor:

$$D_{LB,\alpha\beta} = \begin{pmatrix} D_{LB,xx} + \left(\frac{1}{\omega_-} - \frac{1}{2}\right)(g^{(u)} - 1)u_{LB,x}^2 & D_{LB,xy} + \left(\frac{1}{\omega_-} - \frac{1}{2}\right)(g_{xy}^{(u)} - 1)u_{LB,x}u_{LB,y} \\ D_{LB,xy} + \left(\frac{1}{\omega_-} - \frac{1}{2}\right)(g_{xy}^{(u)} - 1)u_{LB,x}u_{LB,y} & D_{LB,yy} + \left(\frac{1}{\omega_-} - \frac{1}{2}\right)(g^{(u)} - 1)u_{LB,y}^2 \end{pmatrix}. \quad (26)$$

283 We want to resolve the isotropic advection-diffusion equation,  $D_{LB} = D_{LB,xx} =$   
 284  $D_{LB,yy}$  or  $K_{LB} = K_{LB,xx} = K_{LB,yy}$ , with the non-diagonal diffusion tensor  
 285 components set to zero ( $D_{LB,xy} = 0$ ). In contrast to the  $D2Q5$  model, with  
 286  $D2Q9$  it is possible to cancel the numerical diffusion by the proper choice  
 287 of the equilibrium functions, i.e.  $g_{xy}^{(u)} = g^{(u)} = 1$ . The particular choice of  
 288 parameters used in simulations is  $c_e = \frac{1}{3}$ ,  $\Lambda = \frac{1}{4}$ . Thus, the diffusion co-  
 289 efficient in the lattice Boltzmann system  $D_{LB}$  is matched through  $\omega_-$ , i.e.  
 290  $D_{LB} = c_e \left(\frac{1}{\omega_-} - \frac{1}{2}\right) = \frac{1}{3} \left(\frac{1}{\omega_-} - \frac{1}{2}\right)$ . For the particular choice  $\Lambda = \frac{1}{4}$ ,  $\omega_+$  can  
 291 be found easily as  $\omega_+ = 2 - \omega_-$ .

We validated two types of boundary conditions: Inamuro boundary condi-  
 tions [35] and pressure anti bounce-back boundary conditions [39]. However,  
 the simulation results are presented only for pressure anti bounce-back due  
 to their ability to handle complex boundaries in a simple way:

$$f_{B,i}^* = -f_{F,\bar{i}}^* + 2eq^+(C^*, \mathbf{u}_{LB}), \quad (27)$$

292 where  $C^*$  is the concentration to be imposed at the surface,  $\mathbf{u}_{LB}$  is the  
 293 surface velocity,  $i$  is the direction number pointing to the domain located  
 294 at the boundary surface  $B$ ,  $\bar{i}$  is the direction number opposite to  $i$  and is  
 295 located at the fluid node  $F$  specifically so that node  $B$  is located at the  
 296 location  $F + \mathbf{c}_i$ .

297 Note that the parameters of the lattice Boltzmann scheme are connected  
 298 with physical parameters only through non-dimensional numbers govern-

ing the physics of the problem. In our case, this is the Peclet number,  
 $Pe = \frac{U_{\text{bubble}}L}{D}$ . Therefore, one can choose any quantity, for example  $U_{\text{bubble}}$   
in the lattice Boltzmann units ( $u_{\text{LB,bubble}}$ ) as long as the Peclet number is  
matched in physical space and numerical simulations. The fact that  $u_{\text{LB,bubble}}$   
can be varied in certain ranges is extremely useful in the context of numerical  
simulations. This allows to increase the time step and decrease the compu-  
tational demand (by an order of magnitude). This point will be used in the  
simulations and covered later.

The next section will cover LBM benchmarks that resemble the mass  
transfer from a bubble (mass transfer to the liquid with the parabolic velocity  
profile and mass transfer from a cylinder). As soon as we move to numerical  
simulations, all quantities are non-dimensional. Thus, we drop the subscript  
 $LB$  for brevity.

### 3.2. The radial case

The case to be examined is the mass transfer from a circle with radius  
 $a$ , with the circle approximated as a stair-case. It can be described by the  
following system of equations:

$$\begin{aligned}\partial_t C(r, t) &= \frac{1}{r} \partial_r r \partial_r C(r, t) \\ C(a, t) &= C_0, \quad C(r, 0) = C_{\text{init}}\end{aligned}\tag{28}$$

The analytical solution is [47]:

$$\frac{C(r, t) - C_0}{C_{\text{init}} - C_0} = \sum_{n=1}^{\infty} \frac{2}{\mu_n J_1(\mu_n)} \exp\left(-\mu_n^2 \frac{Dt}{a^2}\right) J_0\left(\mu_n \frac{r}{a}\right),\tag{29}$$

where  $\mu_n$  is the  $n$ -th zero root of the 0th order Bessel polynomial  $J_0(\mu_n) = 0$ .  
Some of the corresponding roots are as follows:  $\mu_1 = 2.4048$ ,  $\mu_2 = 5.5201$ ,

$\mu_3 = 8.6537$ ,  $\mu_4 = 11.7915$ ,  $\mu_5 = 14.9309$ . By taking the initial concentration as 0, one obtains:

$$C(r, t) = C_0 \left( 1 - \sum_{n=1}^{\infty} \frac{2}{\mu_n J_1(\mu_n)} \exp\left(-\mu_n^2 \frac{Dt}{a^2}\right) J_0\left(\mu_n \frac{r}{a}\right) \right). \quad (30)$$

Time dependency goes via the non-dimensional time:  $\tau = \frac{Dt}{a^2}$ . The domain size was  $129 \times 129$  with the circle radius  $a = 40$  lattice units. Some results for different diffusion coefficients are presented in Fig.5. The numerical simulations with the bounce-back boundary conditions are able to accurately reproduce the analytical results.

### 3.3. Poiseuille velocity profile

The problem we want to address can be formulated through the following PDE:

$$\begin{aligned} \frac{\partial C}{\partial x} U(y) &= D \frac{\partial^2 C}{\partial y^2} \\ C(0, y) &= 0, \quad C(x, \pm\delta) = C^*, \quad \frac{\partial C}{\partial y}(x, 0) = 0 \\ U(y) &= U_0 \left( 1 - \left( \frac{y}{\delta} \right)^2 \right) \end{aligned} \quad (31)$$

The procedure to solve this problem is presented in Appendix A which yields the final solution as:

$$C = C^* - C^* \sum_{m=0}^{\infty} C_m e^{-m^4 \frac{x}{\delta} \frac{1}{Pe}} e^{-m^2 y^2 / (2\delta^2)} {}_1F_1\left(-\frac{m^2}{4} + \frac{1}{4}, \frac{1}{2}, m^2 \frac{y^2}{\delta^2}\right), \quad (32)$$

where coefficients  $C_m$  are taken from Eq. 48. The comparison between contours of analytical and simulation results is presented in Fig. 6. Parameters were taken as:  $D = 0.0185$ , the grid dimension is  $80 \times 1600$ . The centerline velocity is  $U_0 = 0.05$  which yields the Peclet number  $Pe = U_0 \delta / (2D) = 108.108$ .



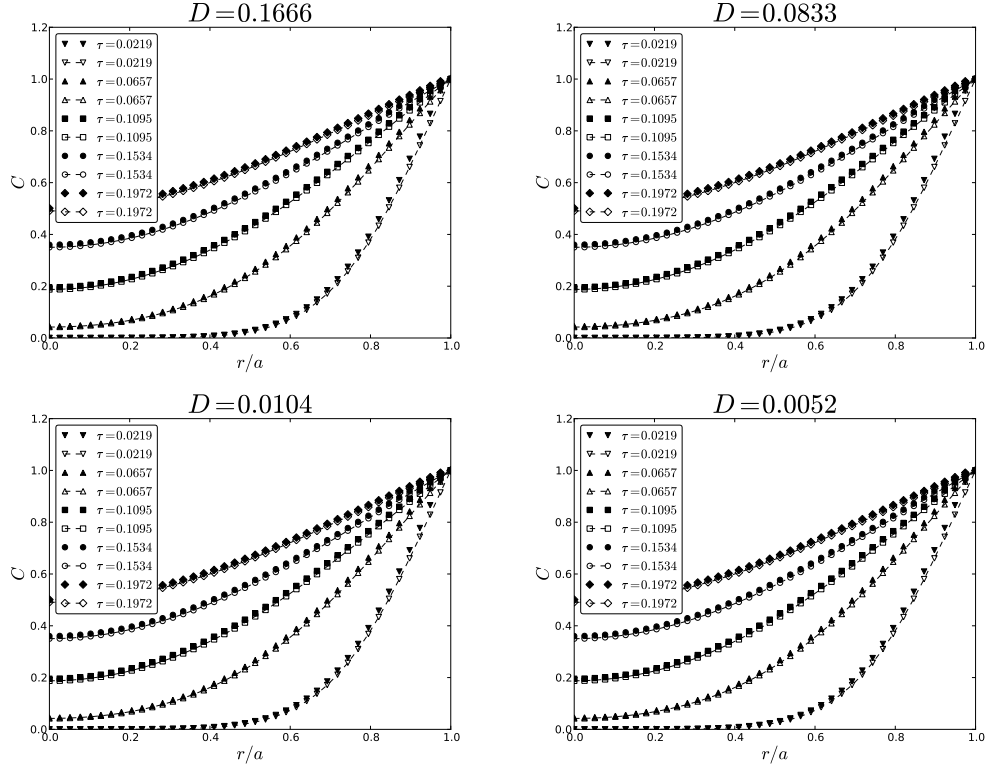


Figure 5: Profiles for different diffusion parameters varied with  $\omega_-$  (lines: Eq. 30, symbols: LB results). One can see that the diffusion from curved boundaries is captured accurately.  $r$  is the distance from the center.

323 The results are in good agreement. The simulations capture accurately the  
 324 singular derivative for  $x = 0$ .

325 Now that the LBM is validated against the benchmarks relevant for the  
 326 flow around bubbles, one can examine the cases mentioned in Section 2.3 to  
 327 calculate the volumetric mass transfer coefficient for the Taylor bubble train  
 328 flow.

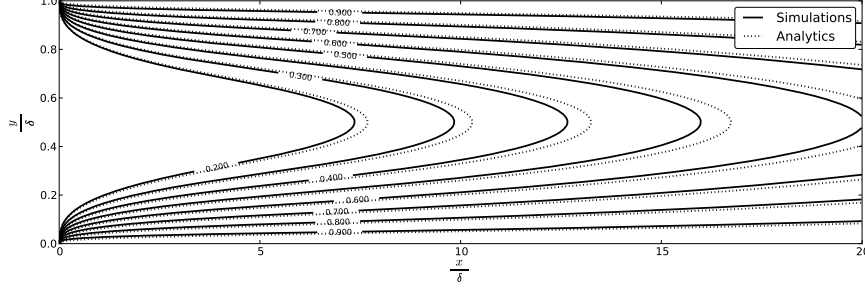


Figure 6: Comparison between the analytical concentration contours and simulations with pressure anti bounce-back conditions, Eq. 27. The simulation was done for  $D_{LB} = 0.0185$  with a  $80 \times 1600$  grid. The centerline velocity is  $U_0 = 0.05$ , and the Peclet number is 108.108.

#### 329 4. Numerical approach

330 A multiphase code was utilized to obtain the flow patterns and bubble  
 331 shapes for different capillary numbers [18]. Five particular cases were cho-  
 332 sen to be examined, their results are summarized in Table 1. Note that  
 333 the velocities (LB system) in Table 1 are small. This means that to match  
 334 large Peclet numbers,  $Pe = \frac{U_{\text{bubble}} L}{D}$ , usually used in experiments, one needs  
 335 to decrease the diffusion coefficient  $D = \frac{1}{3} \left( \frac{1}{\omega_-} - \frac{1}{2} \right)$ . Thus, the parame-  
 336 ter  $\omega_- \approx 0.5$ . However, for such values of  $\omega_-$  the stability of the lattice  
 337 Boltzmann method drastically decreases [45]. On the other hand, one iter-  
 338 ation in the lattice Boltzmann system corresponds to a physical time step  
 339  $\Delta t_{\text{phys}} = U_{\text{bubble, LB}} \frac{\Delta x}{U_{\text{bubble, phys}}}$ , where  $U_{\text{bubble, phys}}$  is the physical velocity [m/s],  
 340 and  $t_{\text{phys}}$  is the physical time step [s]. The iteration time is proportional  
 341 to the velocity  $U_{LB}$  and the typical number of simulation steps to obtain  
 342 the steady-state mass transfer coefficient for  $Ca < 0.2$  is of the order of a  
 343 few million. Therefore, it is desirable to increase  $U_{LB}$  while maintaining the

$Ca$	$Re$	$U_{\text{bubble}}$	$\delta$	$\varepsilon_{\text{gas}}$	$U_{\text{liq}}$	$U_{\text{gas}}$	$L_{\text{bubble}}$	$L_{\text{slug}}$
0.097	1.656	0.0055	0.092	0.30	0.0046	0.0016	5.79	9.21
0.254	4.318	0.0143	0.132	0.28	0.0108	0.0041	6.12	8.88
0.526	8.938	0.0297	0.157	0.27	0.0209	0.0080	6.19	8.81
0.750	12.744	0.0424	0.167	0.25	0.0293	0.0107	5.96	9.04
1.040	17.665	0.0588	0.177	0.22	0.0397	0.0135	5.59	9.41

Table 1: Sample results with the binary liquid lattice Boltzmann model [18]. The following notations are used: the capillary number  $Ca = \frac{U_{\text{bubble}}L}{\rho\nu_{\text{liq}}}$ ,  $U_{\text{liq}}$  is the superficial liquid velocity,  $U_{\text{gas}}$  is the superficial gas velocity,  $\varepsilon_{\text{gas}}$  is the gas holdup.  $\delta$  is the non-dimensional film thickness,  $L_{\text{bubble}}$  and  $L_{\text{slug}}$  are the non-dimensional bubble and slug lengths (defined as multiplies of the channel height). The simulation sketch is presented in Fig. 1.

344 Peclet number. If one increases the velocity, then  $\omega_-$  increases as well, which  
345 impacts positively on the stability of the LBM.

346 Given all the considerations above, mass transfer simulations are per-  
347 formed as follows:

348 **Flow field** Given a capillary number  $Ca$ , one needs to obtain hydrodynamic  
349 fields around the bubble using the multiphase binary liquid lattice  
350 Boltzmann model according to our previous work [18]. Periodic bound-  
351 ary conditions were used in that work. The grid used was  $202 \times 3000$   
352 which corresponds to the fluid domain of size  $200 \times 3000$ . That grid  
353 resolution was taken to ensure grid independency of the results [18].  
354 Note that we do not approximate bubble shapes by correlations, but  
355 directly resolve them using the multiphase solver.

356 **Bubble reference frame** Once the hydrodynamics is solved, the mass trans-

fer simulations are conducted in the reference frame moving with the bubble, where the bubble stands still and the liquid flows around the bubble. We impose a uniform and steady concentration on the surface of the bubble with the anti bounce-back condition, Eq. 27.

**Velocity improvement** One can scale the velocity to perform faster simulations. However, before doing it one needs to improve the velocity field. This issue arises because of the multiphase model used in the flow simulations. The binary liquid lattice Boltzmann model is a diffuse interface model where no clear boundary between gas and liquid exists. We obtain the bubble shape by imposing a condition on the order parameter field  $\phi$  with  $\phi \leq 0$  in the bubble [18]. The velocity of the bubble is defined as the bubble tip velocity. Because of the square grid, the shape of the bubble is determined within an accuracy of one grid spacing. Thus, there is an error in the determination of the bubble velocity. Though these errors are small, there is still a small non-zero velocity component pointing into the bubble in some places, see Fig. 8 in [18] where some streamlines are penetrating the bubble surface. This small velocity is amplified upon the velocity scaling and is inconsistent with the advection-diffusion equation leading to instability after many iterations.

Thus, before performing the mass transfer simulations an additional single phase hydrodynamic simulation is performed. A free-surface solver was developed in order to obtain a velocity field consistent with the advection-diffusion equation. We take results from the multiphase simulations, extract a bubble shape using the phase indicator  $\phi \leq 0$ ,

and approximate the bubble shape by the stair-case line with imposed free-slip boundary condition on it. The bubble velocity is then imposed on the walls. This corresponds to conducting simulations in the reference frame moving with the bubble. Appendix B covers the simple free-slip boundary condition implementation drastically improving velocity patterns. The system is iterated until a steady state is reached and as a result, all non-zero velocity components perpendicular to the bubble surface are completely eliminated. Note, that these types of simulations are much faster than the original multiphase simulations. We compared original multiphase simulations with one-component free-slip simulations. All quantities such as superficial slug and liquid velocities are within 3% for all capillary numbers in the range  $0.05 \leq Ca \leq 1.0$ . One can see in Fig. 7 two streamline profiles for  $Ca = 0.097$  and  $Ca = 1.040$ .

**Mass transfer** After the improved velocity profiles are obtained one can perform any mass transfer simulation with the various boundary conditions as covered in Section 2.3. For this purpose one needs to match the Peclet number  $Pe$  taken from experiments.

## 5. Results

This section covers simulation results. We first examine the possibility to increase the fluid velocity while keeping the Peclet number the same. After that the results for periodic boundary conditions for 5 capillary number cases will be presented. Finally, we will examine many cell simulations for

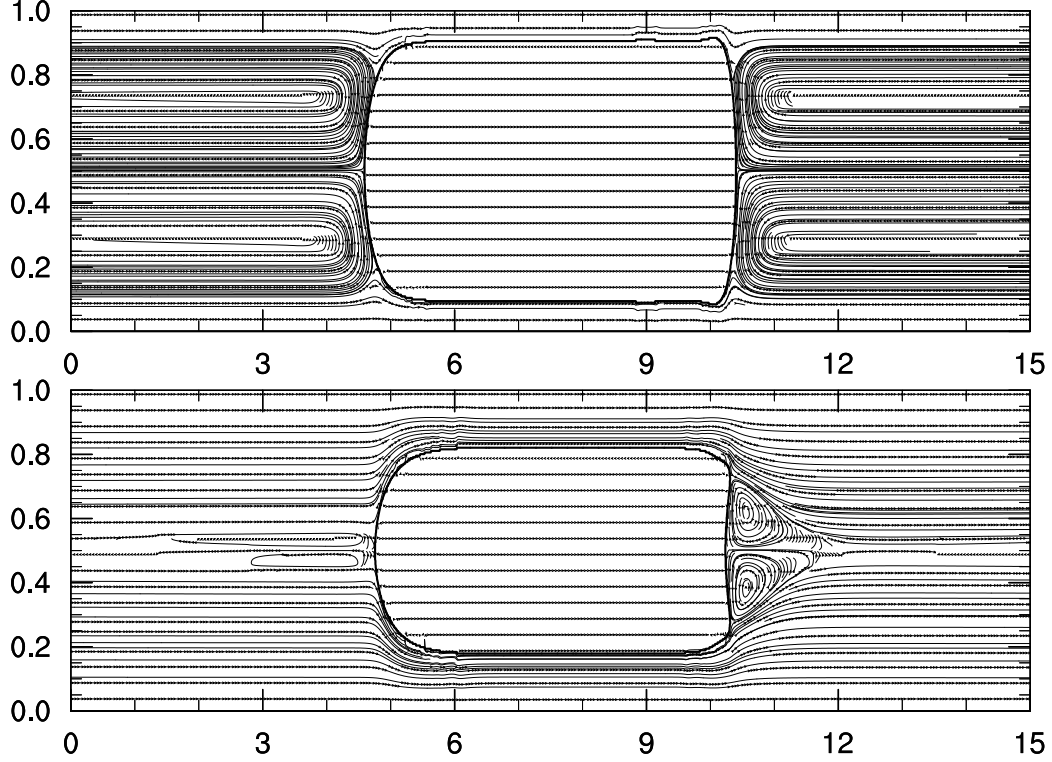


Figure 7: The streamline patterns produced by the free-surface flow solver with simplified approximation of the free-slip bubble surface, see Appendix B. Two completely different velocity patterns are obtained,  $Ca = 0.097$  (top) and  $Ca = 1.040$  (bottom).

two representative velocity patterns related to  $Ca = 0.0907$  and  $Ca = 1.04$  respectively (see Fig. 7).

The simulations were performed using an in-house code with different modifications for different boundary conditions. A typical mass transfer simulation (domain size is  $3000 \times 202$  cells) for  $10^6$  iterations takes around 24 hours on an Intel dual core CPU with the internal clock frequency of 2 GHz. All simulations (serial for one unit cell and parallel for a few unit cells) are done using computers of the WestGRID high-performance clusters in West-

413 ern Canada.

#### 414 5.1. Velocity scaling at constant Peclet number

This section addresses the process of significantly increasing the velocity magnitude while keeping dimensionless parameters the same to speed up simulations. This is especially important to be able to simulate a few unit cells in a reasonable time. For example, ten unit cell simulations require a grid of  $30000 \times 202$  nodes. Since the Peclet number is the only dimensionless quantity governing the advection-diffusion equation:

$$Pe = \frac{U_{\text{bubble}} N_y}{D}. \quad (33)$$

415 one needs to increase the diffusion coefficient when the velocity is increased.  
416 Simulation runs were made with velocities 2, 4, 6, 8, 10, 15, 20, 40 times larger  
417 than the original velocities. The velocities, their corresponding capillary and  
418 Schmidt numbers are presented in Table 2. One can see that the Schmidt  
419 number,  $Sc = Pe/Re \approx 790$ , has a value corresponding to a dye with a low  
420 molecular diffusivity. This is done to minimize the dye diffusion influence on  
421 results but rather study the mass transfer in hydrodynamics patterns pro-  
422 vided by the Taylor bubble flow. Periodic boundary conditions were used and  
423 the mass transfer coefficient was calculated according to Eq. 4. One can see  
424 in Table 2 that for small capillary numbers ( $Ca < 0.2$ ) it is possible to scale  
425 up velocity significantly (20 – 40 times) to obtain a velocity around 0.2 where  
426 simulations are still stable. However, for larger capillary numbers the scale  
427 up is smaller (2 – 4 times), and the velocity for stable simulations is around  
428 0.1. Table 2 shows that the velocity limit for periodic boundary conditions  
429 is 0.1 across all capillary numbers. To be on the safe side, velocities should

not be scaled up beyond that value. It gives us a preliminary idea to what extent one can scale periodic mass transfer simulations. The concentration contour profiles corresponding to Table 2 for different velocity scalings are presented in Fig. 8. One can see an acceptable agreement between the cases with the same Peclet number but different velocity scalings. Note, that the speedup can be up to 10 to 40 times.

### 5.2. Average concentration results

In this section we will examine the case where the volume averaged concentration over time is used as the characteristic concentration. To calculate the volumetric mass transfer coefficient we used Eq. 12. Results for the coefficient  $k_L a \frac{U_{\text{bubble}}}{U_{\text{gas}} + U_{\text{liq}}}$  are shown in Fig. 9 for different capillary, Peclet numbers and velocity scalings indicated in Table 2. When the average concentration gets close to  $C^* = 1$ , Eq. 12 gives inadequate results due to the accuracy of the logarithmic function evaluation. This is the reason that curves in Fig. 9 tend to shoot up for long times. Due to velocity scaling each simulation has a different physical time step. Thus, we normalized time such that it represents a number of unit cell lengths which the bubble has travelled, i.e.  $N_{\text{cell units}} = \frac{\text{scale} \cdot U_{\text{bubble}} \cdot N_{\text{iter}}}{L_{\text{unit}}}$ . Fig. 9 shows the volumetric mass transfer dependency against the distance in unit cell length. One can see in Table 3 that for different Peclet numbers different time (number of unit cells) is required to achieve steady state. For example, for larger Peclet numbers fewer length is required to achieve the steady state condition.

Overall one obtains steady state volumetric mass transfer coefficients for periodic boundaries simulations if the following conditions are fulfilled:

**I** Scaling is performed so that  $U_{\text{max}} = \text{scale} \cdot U_{\text{bubble}} \leq 0.1$ .



455 **II** The larger the Peclet number, the fewer iterations are required. One can  
 456 extrapolate data from Table 3, say  $L_{\text{steady}}$ , and estimate the number of  
 457 iterations to reach the steady-state as  $\text{scale} \cdot U_{\text{bubble}} \cdot N_{\text{iter}} \leq L_{\text{steady}}$ .

### 458 5.3. Periodic boundaries with the inlet/outlet characteristic concentration

459 The volumetric mass transfer coefficient was calculated using Eq. 12 with  
 460 the characteristic concentration being the inlet/outlet flux averaged concen-  
 461 tration as used by van Baten and Krishna [2]. One can see in Fig. 10 that the  
 462 calculated volumetric mass transfer coefficient behaves differently from the  
 463 domain averaged volumetric mass transfer coefficient. For example, for small  
 464 capillary numbers, i.e.  $Ca = 0.097, 0.254, 0.526$  the values are overpredicted  
 465 ( $k_L a \frac{L_{\text{unit}}}{U_{\text{liq}} + U_{\text{gas}}} = 0.3, 0.25, 0.1$ ). When the velocity pattern changes from hav-  
 466 ing a vortex in front of the bubble to not having it, i.e.  $Ca = 0.75, 1.04$   
 467 the calculated values are underpredicted compared to estimates based on  
 468 volume-averaged concentration, i.e.  $k_L a \frac{L_{\text{unit}}}{U_{\text{liq}} + U_{\text{gas}}} = 0.06, 0.04$ . As we will  
 469 see later, the domain-averaged characteristic concentration produces proper  
 470 mass transfer coefficients.

### 471 5.4. Van Baten and Krishna formulation

472 The van Baten and Krishna [2] formulation, Eq. 16, is calculated as the  
 473 change of mass in the domain divided by the time difference. We examined  
 474 two approaches: the characteristic concentration taken to be as the domain  
 475 average and as the flux-averaged input/output concentration. The latter case  
 476 corresponds to [2]. The results are presented in Fig. 11 for  $Ca = 0.097$  and  
 477  $Ca = 1.04$ . One can see that the inlet/outlet flux averaged concentration is  
 478 inconsistent. The reason that van Baten and Krishna [2] obtained the mass

transfer coefficient close to the analytical estimation is that the liquid slug is well mixed ( $Ca < 0.1$  which is below the range studied here) so that the averaged concentration is close to the inlet/outlet concentration.

However, results for the domain-averaged concentration using the approach of van Baten and Krishna are close to simulation results in Section 5.2. Note that for  $Ca = 0.097$  the obtained mass transfer coefficient value is 10% lower than the value in Section 5.2. However, as will be shown later the obtained volumetric mass transfer coefficient for  $Ca = 0.097$  has the same value as for the simulations of a few unit cells. Therefore the approach of van Baten and Krishna [2] produces accurate results if the characteristic concentration is the volume-averaged concentration (not the inlet/outlet flux-averaged concentration used in the original work). From the computational point of view, it also requires the concentration fields in time and space to calculate the mass change in time and the averaged domain characteristic concentration.

#### 5.5. Simulations for several unit cells

In order to achieve independence from the boundary conditions and a closer match with the physical system being modelled, one can simulate several unit cells, corresponding to the head of a bubble train. If end effects are eliminated then the average domain characteristic should change in time according to Eq. 13. This eliminates the ambiguity inherent in choosing a definition of the characteristic concentration, it becomes the same domain-averaged concentration as the one measured in experiments.

This section studies the number of unit cells required for the volumetric mass transfer coefficient to be independent of the influence of boundaries.

504 We chose two different velocity patterns (see Fig. 7 for  $Ca = 0.097$  and  
 505  $Ca = 1.04$ ) to perform the simulations. For  $Ca = 0.097$  we performed  
 506 simulations with 4, 6, 8, 10 cells, and for  $Ca = 1.040$  only with 4, 6, 8 cells.  
 507 We observed however that simulations with a domain length of 10 unit cells  
 508 produce the same results as those with 8 unit cells.

509 We keep velocity in the range  $0.05 - 0.1$  to avoid excessively long simula-  
 510 tion times. The number of steps for mass to pass through the whole domain  
 511 can be approximated as  $1.5 \frac{L_{\text{unit}}}{U_{\text{bubble}}}$ , which takes into account the bulk veloc-  
 512 ity. If  $U_{\text{bubble}}$  is taken as 0.05 then for the domain size  $L_{\text{unit}} = 3000$  one can  
 513 obtain the following number of iterations for the mass to cross the unit cell  
 514  $1.5 \frac{3000}{0.05} = 90000$ . Therefore,  $10^6$  iterations are enough for a system consisting  
 515 of 10 unit cells. For more accurate estimations of the number of time steps  
 516 depending on the Peclet number we refer to Section 5.1.

## 517 5.6. $Ca = 0.097$ results

There are two characteristics we want to track in the simulations: the average concentration in the unit cell with time (see Eq. 13), and the accumulated mass rate in the domain which takes into account inlet/outlet fluxes (see Eq. 18). The former resembles experiments: if one has a large enough number of unit cells, then the averaged domain concentration should change in time according to Eq. 13:

$$k_L a \frac{L_{\text{unit}}}{U_{\text{gas}} + U_{\text{liq}}} = \frac{L_{\text{unit}}}{U_{\text{bubble}}(t_2 - t_1)} \ln \left( \frac{C^* - \langle C(t_1) \rangle}{C^* - \langle C(t_2) \rangle} \right) \quad (34)$$

518 The non-dimensional volumetric mass transfer coefficient calculated based on  
 519 Eq. 34 (domain-averaged concentration change in time) is represented in Fig.  
 520 12 for different unit cells. One can see that mass transfer coefficient values are

521 the same as the mass flux concentration based on the van Baten and Krishna  
 522 formulation with the characteristic concentration being the domain-averaged  
 523 concentration (see Section 5.4). This demonstrates two things: the domain-  
 524 averaged concentration is the only choice for the characteristic concentration,  
 525 and periodic boundary conditions for one unit cell produce good results.

In comparison with periodic boundary conditions Eq. 18 allows to calculate the mass transfer coefficient differently. Eq. 18 can be rewritten as:

$$k_L a \frac{L_{\text{unit}}}{U_{\text{liq}} + U_{\text{gas}}} = \frac{L_{\text{unit}}}{U_{\text{gas}} + U_{\text{bubble}}} \frac{V \frac{\langle C(t_2) \rangle - \langle C(t_1) \rangle}{t_2 - t_1}}{\frac{- \int C_{\text{outlet}}(L_{\text{unit}}, y, t^*) u(L_{\text{unit}}, y) dy + \int C_{\text{inlet}}(0, y, t^*) u(0, y) dy}{V(C^* - \langle C(t^*) \rangle)}}, \quad (35)$$

526 where  $t^*$  is the mean between  $t_1$  and  $t_2$ .

527 Fig. 13 shows average concentrations in different units and  $k_L a \frac{L_{\text{unit}}}{U_{\text{liq}} + U_{\text{gas}}}$   
 528 based on Eq. 35 calculated for each unit for velocity scale 10 and 6 unit cells  
 529 (all velocity scales produce the same results). It shows that the volumetric  
 530 mass transfer coefficient is consistent for internal segments, i.e. unit cells  
 531 numbers 2 – 4. The results for the volumetric mass transfer coefficient calculated by Eq. 18 for multiple unit cells are close (less than 10% deviation) to  
 532 results for periodic boundary conditions in Section 5.2. The same dependencies can be found for 8 and 10 unit cells simulations but we do not present  
 533 them here. We also do not present 4 unit cells simulation results which are  
 534 highly influenced by entrance and exit effects.  
 535

536 The calculation of the volumetric mass transfer coefficient is more difficult  
 537 using Eq. 35. However, it will be shown below that this equation can be  
 538 significantly simplified in case of larger capillary numbers ( $Ca > 0.7$ ).  
 539

The same correlations were examined for a different velocity pattern at  $Ca = 1.040$ . The original Peclet number we started with is  $Pe = 14041$  (Table 2). To avoid stability problems of the lattice Boltzmann method we changed the original Peclet number by increasing diffusion to  $Pe = 2644$  (corresponding Schmidt number  $Sc = 709.84/5 = 158.96$ ). Our goal is to understand the influence of velocity pattern, not to perform simulations with a certain Peclet number. Thus, we have a certain degree of freedom to vary the simulations' Peclet number. This is achieved by adjusting velocity and diffusion coefficients. For example, if the velocity scaling is 2, then by increasing the initial diffusion coefficient 10 times one will eventually obtain a Peclet number 5 times smaller than the initial Peclet number. The results with respect to the number of unit cells are the same as for  $Ca = 0.097$ : at least 6 unit cells are required to avoid the influence of inlet/outlet effects. Thus, only 6 unit cells results are presented in Fig. 14 which shows the average concentration for each unit cell. One can see that the average volume concentration for each unit cell converges to a constant value. Thus, all the mass generated by the bubble is transferred through the boundaries. This indicates that the liquid slug is unmixed since no concentration travels back to inlet with the vortex and increases the average concentration in each unit cell. Note that the periodic boundary conditions cannot show whether the liquid slug is mixed or not due to the fact that the averaged domain concentration always increases in time. Thus, the volumetric mass transfer coefficient  $k_L a \frac{L_{\text{unit}}}{U_{\text{liq}} + U_{\text{gas}}}$  can be calculated according to the definition, Eq. 18:

$$k_L a = \frac{\dot{m} - \int C_{\text{outlet}}(y)u(L_{\text{unit}}, y)dy + \int C_{\text{inlet}}(y)u(L_{\text{unit}}, y)dy}{V(C^* - \langle C(t) \rangle)}, \quad (36)$$

541 where  $V$  is the unit cell volume. There is no accumulated mass in the domain,  
542 so  $\dot{m} = 0$ . Like periodic boundary conditions, this case is another extreme  
543 limit of Eq. 18. Note that to calculate the volumetric mass transfer coefficient  
544 one needs only the spatial information and does not require the knowledge of  
545 how the averaged concentration changes in time, which significantly lowers  
546 storage requirements for the simulations with  $Ca > 0.7$  where there is no  
547 vortex in the liquid slug.

548 Fig. 15 (bottom) shows the volumetric mass transfer coefficient based  
549 on spatial calculations of inlet/outlet concentrations. One can see that the  
550 volumetric mass transfer coefficient is close to the calculated volumetric mass  
551 transfer coefficient using the time averaged approach and periodic boundaries  
552 one unit cell simulations (presented in the same figure for comparison). Note  
553 that results for approaches which incorporate the volume-averaged character-  
554 istic concentration either for one cell or a few unit cells coincide. Therefore,  
555 for certain hydrodynamic patterns ( $Ca > 0.7$ ), one can easily convert time  
556 domain to spatial domain calculations using simulations of several unit cells.

557

## 558 5.8. Comparison of experimental and analytical correlations

While the goal of this paper is not to compare simulation results with the  
experimental measurements, we felt that a short note about such compari-  
son will be beneficial. Unfortunately, to the authors' knowledge, there are no  
reported experimental results measuring the mass flux for bubbles flowing be-  
tween parallel plates. However, an interesting correlation for the volumetric  
mass transfer coefficient was presented by Yue et al. [7] for three-dimensional

microchannel geometries:

$$k_L a = \frac{2}{d_h} \left( \frac{DU_{\text{bubble}}}{L_{\text{bubble}} + L_{\text{slug}}} \right)^{0.5} \left( \frac{L_{\text{bubble}}}{L_{\text{bubble}} + L_{\text{slug}}} \right)^{0.3}$$

$$k_L a \frac{L_{\text{unit}}}{U_{\text{gas}} + U_{\text{liq}}} = 2 \frac{L_{\text{unit}}}{d_h} \left( \frac{D}{L_{\text{unit}}(U_{\text{bubble}} + U_{\text{gas}})} \frac{U_{\text{bubble}}}{U_{\text{gas}} + U_{\text{liq}}} \right)^{0.5} \left( \frac{L_{\text{bubble}}}{L_{\text{bubble}} + L_{\text{slug}}} \right)^{0.3} \propto Pe^{-\frac{1}{2}} \quad (37)$$

One can see that the volumetric mass transfer correlation should be approximately proportional to  $Pe^{-0.5}$ . One can also use analytical estimates of the volumetric mass transfer coefficient calculated using the Higbie penetration theory [17]. One can derive the analytical expression for the mass transfer for bubble train flow between parallel plates by following the works [16, 2]:

$$k_L a \frac{L_{\text{unit}}}{U_{\text{liq}} + U_{\text{gas}}} = \frac{L_{\text{unit}}}{U_{\text{gas}} + U_{\text{liq}}} \left( 4 \sqrt{DU_{\text{bubble}}} \pi \frac{\sqrt{L_{\text{bubble}} - H(1 - 2\delta)}}{L_{\text{unit}}H} \right. \\ \left. + 2\sqrt{2} \sqrt{DU_{\text{bubble}}} \frac{\sqrt{H(1 - 2\delta)}}{L_{\text{unit}}H} \right), \quad (38)$$

where  $H$  is the channel height, and  $\delta$  is the non-dimensional film thickness (in channel heights).

Fig. 16 shows a comparison between the correlation by Yue et al. [7], the analytical expression, Eq. 38, and the current simulation results presented in Table 3. The coefficients are close to each other, especially given that the correlation by Yue et al. [7] is for three-dimensional cases. The fitting procedure based on the results of this work showed that the power of the Peclet number dependence is  $-0.50038$  which is close to the theoretical value  $-0.5$ . The fitting curve is  $7.745Pe^{-0.50038}$ .

## 6. Summary

This work examines a way to calculate the volumetric mass transfer coefficient of Taylor/Batchelor bubble train flow in the framework of the lattice

Boltzmann method. The volumetric mass transfer for the Taylor/Batchelor  
 bubble train flow can be relatively easily estimated by measuring concen-  
 trations of a scalar along the streamwise direction. In comparison with the  
 continuous nature of experiments, i.e. where one doesn't distinguish bubbles,  
 the numerical simulations are performed with a small number of discrete unit  
 cells, each containing a bubble. This work bridges the continuous nature of  
 experiments and a few unit cells simulations performed in the reference frame  
 moving with the bubble. We thoroughly performed and examined simulations  
 with different definitions of the volumetric mass transfer coefficient and char-  
 acteristic concentration, i.e. domain-averaged or flux-averaged inlet/outlet  
 concentrations, for different hydrodynamic patterns seen in the bubble train  
 flow. We also performed open inlet/outlet mass transfer simulations for a  
 few unit cells to resemble the continuous picture seen in experiments. By  
 thorough comparison it was shown that the easiest recipe is to perform sim-  
 ulations with periodic boundary conditions and calculate the volumetric mass  
 transfer coefficient based on the domain-averaged concentration through any  
 formulation (van Baten and Krishna, periodic boundary conditions, simu-  
 lations of several unit cells) as they produce consistent results. The best  
 accuracy in terms of closeness to the results of simulations of several unit  
 cells (continuous picture seen in experiments) is achieved with formulations  
 based on the mass difference or on the domain-averaged concentrations taken  
 in different times, Eq. 13. Eq. 11 gives a slightly overestimated volumet-  
 ric mass transfer coefficients (less than 10%). The original formulation of  
 van Baten and Krishna [2] is inconsistent if one takes the inlet/outlet flux-  
 averaged concentration to be the characteristic concentration as in their orig-



596 inal work. Simulations of several unit cells are harder to perform, but they  
597 provide a good reference point since they more closely resemble the continu-  
598 ous nature of the bubble train flow. In addition, simulations of several unit  
599 cells indicate how well the liquid slug is mixed. This can be used for velocity  
600 patterns related to  $Ca \geq 0.7$  (weak liquid slug mixing) which allows to cal-  
601 culate the volumetric mass transfer coefficient based on the spatial location  
602 only, without requiring the time snapshots of domain concentration values  
603 used in all other approaches. Finally, a sample of results was compared with  
604 the experimental correlation of Yue et al. [7] and shown to be consistent.

## 605 7. Acknowledgements

606 M.J. acknowledges a scholarship from the TWING project co-financed  
607 by the European Social Fund. A.K. wants to thank Schlumberger for their  
608 financial support.

## 609 A. Mass transfer for planar Poiseuille flow

Close to the previous example but with a different velocity profile, the problem can be formulated through the following PDE:

$$\begin{aligned} \frac{\partial C}{\partial x} U(y) &= D \frac{\partial^2 C}{\partial y^2} \\ C(0, y) &= 0, C(x, \pm\delta) = C^*, \frac{\partial C}{\partial y}(x, 0) = 0 \\ U(y) &= U_0 \left(1 - \left(\frac{y}{\delta}\right)^2\right) \end{aligned} \quad (39)$$

The following substitution simplifies the form of equations:

$$\begin{aligned} \zeta &= \frac{x}{\delta} \frac{D}{U_0 \delta} = \frac{1}{Pe} \frac{x}{\delta} \\ \xi &= \frac{y}{\delta}. \end{aligned} \quad (40)$$

Then the following equation can be obtained:

$$\begin{aligned}\frac{\partial \Theta}{\partial \zeta}(1 - \xi^2) &= \frac{\partial^2 C}{\partial \xi^2} \\ \Theta(\zeta, \xi) &= C - C^* \Theta(0, \xi) = -C^* \Theta(0, \pm 1) = 0\end{aligned}\tag{41}$$

After separation of variables,  $\Theta(\zeta, \xi) = X(\zeta)Y(\xi)$  one can come up with two equations:

$$\begin{aligned}\frac{dX(\zeta)}{d\zeta} + m^4 X(\zeta) &= 0 \\ \frac{d^2 Y(\xi)}{d\xi^2} + m^4(1 - \xi^2)Y(\xi) &= 0\end{aligned}\tag{42}$$

The first equation has a solution:

$$X(\zeta) = \exp(-m^4 \zeta)\tag{43}$$

The second equation can be simplified after substitution  $\bar{\xi} = m\sqrt{2}\xi$  to the standard equation:

$$Y'' - \left(\frac{1}{4}\bar{\xi}^2 + a\right)Y = 0,\tag{44}$$

where  $Y' = dY/d\bar{\xi}$ , and  $a = -m^2/2$ . The equation above has two solutions via parabolic cylinder functions or through the confluent hypergeometric function [48]:

$$\begin{aligned}Y_1 &= e^{-\bar{\xi}^2/4} {}_1F_1\left(\frac{a}{2} + \frac{1}{4}, \frac{1}{2}, \frac{\bar{\xi}^2}{2}\right) \\ Y_2 &= e^{-\bar{\xi}^2/4} {}_1F_1\left(\frac{a}{2} + \frac{3}{4}, \frac{3}{2}, \frac{\bar{\xi}^2}{2}\right)\end{aligned}\tag{45}$$

Taking symmetry conditions into consideration by leaving only the even solution, Eq. 42 has the following solution:

$$Y_m = C_m e^{-m^2 \xi^2/2} {}_1F_1\left(-\frac{m^2}{4} + \frac{1}{4}, \frac{1}{2}, m^2 \xi^2\right)\tag{46}$$

To satisfy the boundary condition we need to find zeros of the hypergeometric function, i.e.  ${}_1F_1\left(-\frac{m^2}{4} + \frac{1}{4}, \frac{1}{2}, m^2\right) = 0$ . First ten eigenvalues can be found

using numerical methods: 1.2967, 2.3811, 3.1093, 3.6969, 4.2032, 4.6548, 5.0662, 5.4467, 5.8023, 6.1373. One needs to satisfy one more condition to obtain coefficients  $C_m$ :

$$-C^* = \sum_m C_m e^{-m^2 \xi^2 / 2} {}_1F_1\left(-\frac{m^2}{4} + \frac{1}{4}, \frac{1}{2}, m^2 \xi^2\right) \quad (47)$$

One can multiply both parts on  $(1 - \xi^2) {}_1F_1\left(-\frac{m^2}{4} + \frac{1}{4}, \frac{1}{2}, m^2 \xi^2\right)$  and through orthogonality (Stourm-Liouville theorem) obtain coefficients:

$$C_m = -C^* \frac{\int_{\xi=0}^1 (1 - x^2) e^{-m^2 \xi^2 / 2} {}_1F_1\left(-\frac{m^2}{4} + \frac{1}{4}, \frac{1}{2}, m^2 \xi^2\right) d\xi}{\int_{\xi=0}^1 (1 - \xi^2) e^{-m^2 \xi^2 / 2} {}_1F_1\left(-\frac{m^2}{4} + \frac{1}{4}, \frac{1}{2}, m^2 \xi^2\right)^2 d\xi} \quad (48)$$

Therefore the complete solution can be written as:

$$C = C^* - C^* \sum_{m=0} C_m e^{-m^4 \frac{x}{\delta} \frac{1}{Pe}} e^{-m^2 y^2 / (2\delta^2)} {}_1F_1\left(-\frac{m^2}{4} + \frac{1}{4}, \frac{1}{2}, m^2 \frac{y^2}{\delta^2}\right), \quad (49)$$

610 where coefficients  $C_m$  are taken from Eq. 48. For the case  $C^*$ , the first ten  
611 coefficients are: 1.2008,  $-0.2991$ ,  $0.1608$ ,  $-0.1074$ ,  $0.0796$ ,  $-0.0627$ ,  $0.0515$ ,  
612  $-0.0435$ ,  $0.0375$ ,  $-0.0329$ .

## 613 B. Free surface boundary conditions

614 There are a few implementations of free boundary conditions [49, 50].  
615 However, we developed the easy solver to impose the free surface boundary  
616 conditions at the complicated surface of the bubble. The reason is to impose  
617 the symmetric boundary conditions. Because the boundary is a staircase ap-  
618 proximation, one can find the normal to the boundary which is always located  
619 by the angle of multiple of 45 degrees, see Fig. 17. The finding identification

620 of normals can be done automatically by a simple code. Imposing the sym-  
 621 metric boundary conditions requires  $U_{n,F} = -U_{n,B}$  and  $U_{\tau,F} = U_{\tau,B}$ . We can  
 622 copy populations in a certain order to do it, for example  $f_{B,i} = f_{F,\bar{i}}$ , where  
 623  $c_i$  and  $c_{\bar{i}}$  are complementary directions, where  $c_{i,n} = -c_{\bar{i},n}$  and  $c_{i,\tau} = c_{\bar{i},\tau}$ ,  
 624 where  $c_{i,n} = (\mathbf{c}_i \cdot \mathbf{n})\mathbf{n}$  and  $c_{i,\tau} = \mathbf{c}_i - (\mathbf{c}_i \cdot \mathbf{n})\mathbf{n}$ . One can check by taking the  
 625 definition of velocity  $\rho\mathbf{u} = \sum_i f_i \mathbf{c}_i$  and substituting it in the relationships  
 626 above, that the normal velocities are canceled, i.e.  $U_{n,F} = -U_{n,B}$ , but the  
 627 tangential velocity component is conserved,  $U_{\tau,F} = U_{\tau,B}$ .

## 628 References

- 629 [1] M.D. Giavedoni and F.A. Saita. The axisymmetric and plane cases of  
 630 a gas phase steadily displacing a Newtonian liquid - A simultaneous  
 631 solution of the governing equations. *Phys. Fluids*, 9(8):2420–2428, 1997.
- 632 [2] J.M. van Baten and R. Krishna. CFD simulations of mass transfer from  
 633 Taylor bubbles rising in circular capillaries. *Chem. Eng. Sci.*, 59:2535–  
 634 2545, 2004.
- 635 [3] M.T. Kreutzer, F. Kapteijn, J.A. Moulijn, and J.J. Heiszwolf. Multi-  
 636 phase monolith reactors: Chemical reaction engineering of segmented  
 637 flow in microchannels. *Chem. Eng. Sci.*, 60:5895–5916, 2005.
- 638 [4] G. Bercic and A. Pintar. The role of gas bubbles and liquid slug lengths  
 639 on mass transport in the Taylor flow through capillaries. *Chem. Eng.*  
 640 *Sci.*, 52(21-22):3709–3719, 1997.
- 641 [5] F.P. Bretherton. The motion of long bubbles in tubes. *J Fluid Mech.*,  
 642 10(2):166–188, 1960.

- 643 [6] G.I. Taylor. Deposition of a viscous fluid on the wall of a tube. *J. Fluid*  
644 *Mech.*, 10:161–165, 1961.
- 645 [7] J. Yue, L. Luo, Y. Gonthier, G. Chen, and Q. Yuan. An experimen-  
646 tal study of air-water Taylor flow and mass transfer inside square mi-  
647 crochannels. *Chem. Eng. Sci.*, 64:3697–3708, 2009.
- 648 [8] R. Gupta, D.F. Fletcher, and B.S. Haynes. Taylor Flow in Microchan-  
649 nels: A Review of Experimental and Computational Work. *J. Comput.*  
650 *Multiphase Flows*, 2:1–32, 2010.
- 651 [9] M.T. Kreutzer, M.G. van der Eijnded, F. Kapteijn, J.A. Moulijn, and  
652 J.J. Heiszwolf. The pressure drop experiment to determine slug lengths  
653 in mulitphase monoliths. *Catalysis Today*, 105:667–672, 2005.
- 654 [10] W.B. Kolb and R.L. Cerro. Film Flow in the Space between a Circular  
655 Bubble and a Square tube. *J. Coll. Int. Sci.*, 159:302–311, 1993.
- 656 [11] T.C. Thulasidas, M.A. Abraham, and R.L. Cerro. Bubble-train flow in  
657 capillaries of circular and square cross section. *Chem. Eng. Sci.*, 50(2):  
658 183–199, 1995.
- 659 [12] D. Liu and S. Wang. Hydrodynamics of Taylor flow in noncircular  
660 capillaries. *Chem. Eng. and Processing*, 47:2098–2106, 2008.
- 661 [13] A. Kuzmin, M. Januszewski, D. Eskin, F. Mostowfi, and J. Derksen.  
662 Three-dimensional binary-liquid lattice boltzmann simulation of mi-  
663 crochannels with rectangular cross sections. *Chem. Eng. J.*, 178:306–  
664 316, 2011.

- 665 [14] A.L. Hazel and M. Heil. The steady propagation of a semi-infinite bubble  
666 into a tube of elliptical or rectangular cross-section. *J. Fluid Mech.*, 470:  
667 91–114, 2002.
- 668 [15] O. Keskin, M. Worner, M. Soghan, T. Bauer, O. Deuchmann, and  
669 R. Lange. Viscous Co-Current Downward Taylor Flow in a Square Mini-  
670 Channel. *AIChE J.*, 56(7):1693–1702, 2010.
- 671 [16] S. Irandoust, S. Ertle, and B. Andersson. Gas-Liquid Mass Transfer in  
672 Taylor Flow Through a Capillary. *Canadian J. Chem. Eng.*, 70:115–119,  
673 1992.
- 674 [17] R. Higbie. The rate of absorption of a pure gas into a still liquid during  
675 short periods of exposure. *Trans. Amer. Inst. Chem. Eng.*, 31:365–389,  
676 1935.
- 677 [18] A. Kuzmin, M. Januszewski, D. Eskin, F. Mostowfi, and J. Derksen.  
678 Simulations of gravity-driven flow of binary liquids in microchannels.  
679 *Chem. Eng. J.*, 171(2):646–654, 2011.
- 680 [19] A. Onea, M. Worner, and D. Cacuci. A qualitative computational study  
681 of mass transfer in upward bubble train flow through square and rect-  
682 angular mini-channels. *Chem. Eng. Sci.*, 64(7):1416–1435, 2009.
- 683 [20] U. Frisch, D. d’Humières, B. Hasslacher, P. Lallemand, Y. Pomeau, and  
684 J.-P. Rivet. Lattice gas hydrodynamics in two and three dimensions.  
685 *Complex Systems*, 1:649–707, 1987.
- 686 [21] G.R. McNamara and G. Zanetti. Use of the Boltzmann Equation to

- 687 Simulate Lattice-Gas Automata. *Phys. Rev. Lett.*, 61(20):2332–2335,  
688 1988.
- 689 [22] F.J. Higuera and J. Jimenez. Boltzmann Approach to Lattice Gas Sim-  
690 ulations. *Europhys. Lett.*, 9(7):663–668, 1989.
- 691 [23] F.J. Higuera, S. Succi, and R. Benzi. Lattice gas dynamics with en-  
692 hanced collisions. *Europhys. Lett.*, 9(4):345–349, 1989.
- 693 [24] D. Yu, R. Mei, L.-S. Luo, and W. Shyy. Viscous flow computations  
694 with the method of lattice Boltzmann equation. *Progress in Aerospace*  
695 *Sciences*, 39:329–367, 2003.
- 696 [25] X. Shan and H. Chen. Simulation of nonideal gases and gas-liquid phase  
697 transitions by the lattice Boltzmann Equation. *Phys. Rev. E*, 49(4):  
698 2941–2948, 1994.
- 699 [26] M.R. Swift, W.R. Osborn, and J.M. Yeomans. Lattice Boltzmann Sim-  
700 ulation of Nonideal Fluids. *Phys. Rev. Lett.*, 75(5):831–834, 1995.
- 701 [27] A.K. Gunstensen, D.H. Rothman, S. Zaleski, and G. Zanetti. Lattice  
702 Boltzmann model of immiscible fluids. *Phys. Rev. A*, 43(8):4320–4327,  
703 1991.
- 704 [28] P. Yuan and L. Schaefer. A Thermal Lattice Boltzmann Two-Phase  
705 Flow Model and Its Application to Heat Transfer Problems -Part 2.  
706 Integration and Validation. *J. Fluids Eng.*, 128:151–156, 2006.
- 707 [29] R. Zhang and H. Chen. Lattice Boltzmann method for simulations of  
708 liquid-vapor thermal flows. *Phys. Rev. E*, 67(066711):1–6, 2003.

- 709 [30] P.J. Dellar. Lattice Kinetic Formulation for Ferrofluids. *J. Stat. Phys.*,  
710 121:105–118, 2005.
- 711 [31] G. Falcucci, G. Chiatti, S. Succi, A.A. Mohamad, and A. Kuzmin. Rup-  
712 ture of a ferrofluid droplet in external magnetic fields using a single-  
713 component lattice Boltzmann model for nonideal fluids. *Phys. Rev. E*,  
714 79(056706):1–5, 2009.
- 715 [32] I. Ginzburg. Equilibrium-type and link-type lattice Boltzmann models  
716 for generic advection and anisotropic-dispersion equation. *Adv. Wat.*  
717 *Res.*, 28:1171–1195, 2005.
- 718 [33] I. Ginzburg. Generic boundary conditions for lattice Boltzmann models  
719 and their application to advection and anisotropic dispersion equations.  
720 *Adv. Wat. Res.*, 28:1196–1216, 2005.
- 721 [34] I. Ginzburg. Variably saturated flow described with the anisotropic  
722 Lattice Boltzmann methods. *Comput. Fluids*, 35:831–848, 2006.
- 723 [35] M. Yoshino and T. Inamuro. Lattice Boltzmann simulations for flow and  
724 heat/mass transfer problems in a three-dimensional porous structure.  
725 *Int. J. Num. Meth. Fluids*, 43:183–198, 2003.
- 726 [36] J.J. Derksen. Simulations of lateral mixing in cross-channel flow. *Com-*  
727 *put. Fluids*, 39:1058–1069, 2010.
- 728 [37] P. L. Bhatnagar, E. P. Gross, and M. Krook. A Model for Collision  
729 Processes in Gases. I. Small Amplitude Processes in Charged and Neutral  
730 One-Component Systems. *Phys. Rev.*, 94(3):511–525, 1954.



- 731 [38] I. Ginzburg, F. Verhaeghe, and D. d’Humières. Two-relaxation-time  
732 Lattice Boltzmann scheme: about parametrization, velocity, pressure  
733 and mixed boundary conditions. *Commun. Comput. Phys.*, 3(2):427–  
734 478, 2008.
- 735 [39] I. Ginzburg and D. d’Humières. Multireflection boundary conditions for  
736 lattice Boltzmann models. *Phys. Rev. E*, 68(066614):1–30, 2003.
- 737 [40] I. Ginzburg. Lattice Boltzmann modeling with discontinuous collision  
738 components: Hydrodynamic and Advection-Diffusion Equations. *J.*  
739 *Stat. Phys.*, 126(1):157–206, 2007.
- 740 [41] D. d’Humières and I. Ginzburg. Viscosity independent numerical errors  
741 for Lattice Boltzmann models: From recurrence equations to ”magic”  
742 collision numbers. *Comp. Math. Appl.*, 58(5):823–840, 2009.
- 743 [42] B. Servan-Camas and F. T.-C. Tsai. Lattice Boltzmann method with two  
744 relaxation times for advection-diffusion equation: Third order analysis  
745 and stability analysis. *Adv. Wat. Res.*, 31:1113–1126, 2008.
- 746 [43] I. Ginzburg. Consistent Lattice Boltzmann schemes for the Brinkman  
747 model of porous flow and infinite Chapman-Enskog expansion. *Phys.*  
748 *Rev. E*, 77(066704):1–12, 2008.
- 749 [44] I. Ginzburg, D. D’Humières, and A. Kuzmin. Optimal Stability of  
750 Advection-Diffusion Lattice Boltzmann Models with Two Relaxation  
751 Times for Positive/Negative Equilibrium. *J. Stat. Phys.*, 139(6):1090–  
752 1143, 2009.

- 753 [45] A. Kuzmin, I. Ginzburg, and A.A. Mohamad. The role of the kinetic pa-  
754 rameter in the stability of two-relaxation-time advection-diffusion lattice  
755 Boltzmann schemes. *Comp. Math. Appl.*, 61:3417–3442, 2011.
- 756 [46] S. Chapman and T.G. Cowling. *The mathematical theory of non-uniform*  
757 *gases*. Cambridge University Press, Cambridge, third edition, 1995.
- 758 [47] A.D. Polyanin, A.M. Kutepov, A.V. Vyazmin, and D.A. Kazenin. *Hy-*  
759 *drodynamics, Mass and Heat Transfer in Chemical Engineering*. Taylor  
760 and Francis, 2002.
- 761 [48] M. Abramowitz and I. Stegun, editors. *Handbook of mathematical func-*  
762 *tions with formulas, graphs and mathematical tables*. National Bureau  
763 of Standards, 1964.
- 764 [49] I. Ginzburg and K. Steiner. A free-surface lattice Boltzmann method  
765 for modelling the filling of expanding cavities by Bingham fluids. *Phil.*  
766 *Trans. R. Soc. Lond. A*, 360:453–466, 2002.
- 767 [50] X. Yin, D.L. Koch, and R. Verberg. Lattice-Boltzmann method for sim-  
768 ulating spherical bubbles with no tangential stress boundary conditions.  
769 *Phys. Rev. E*, 73:1–13, 2006.

Scale	$U_{bubble}$	$\omega_-$	Time Iterations	$C_{aver}$
-------	--------------	------------	-----------------	------------

$$Ca = 0.097, Pe = 1313, Sc = 792.87$$

2	0.011	1.98	400000	0.318
4	0.023	1.96	200000	0.319
8	0.044	1.92	100000	0.320
10	0.055	1.90	80000	0.321
20	0.11	1.81	40000	0.324
40	0.22	1.66	20000	0.328

$$Ca = 0.254, Pe = 3414, Sc = 790.64$$

2	0.0286	1.98	800000	0.6533
4	0.0572	1.96	400000	0.6591
8	0.1144	1.92	200000	0.6692
10	0.1430	1.90	160000	0.6734
20	0.2860	1.81	80000	0.6894

$$Ca = 0.526, Pe = 7092, Sc = 793.46$$

2	0.0594	1.98	200000	0.3271
4	0.1188	1.96	100000	0.3315

$$Ca = 0.750, Pe = 10125, Sc = 794.49$$

2	0.0848	1.98	200000	0.3489
---	--------	------	--------	--------

$$Ca = 1.040, Pe = 14041, Sc = 794.84$$

2	0.1176	1.98 <sup>51</sup>	200000	0.3675
---	--------	--------------------	--------	--------

Table 2: Indications of the achievable stable velocity  $U_{bubble}$  when one scales velocity. Since the physical time step represented by a single iteration of the simulation is directly proportional  $U_{bubble, LB}$ , scaling the velocity directly translates to an effective speed-up of the simulation. Note that time iterations indicated in the table correspond to the same

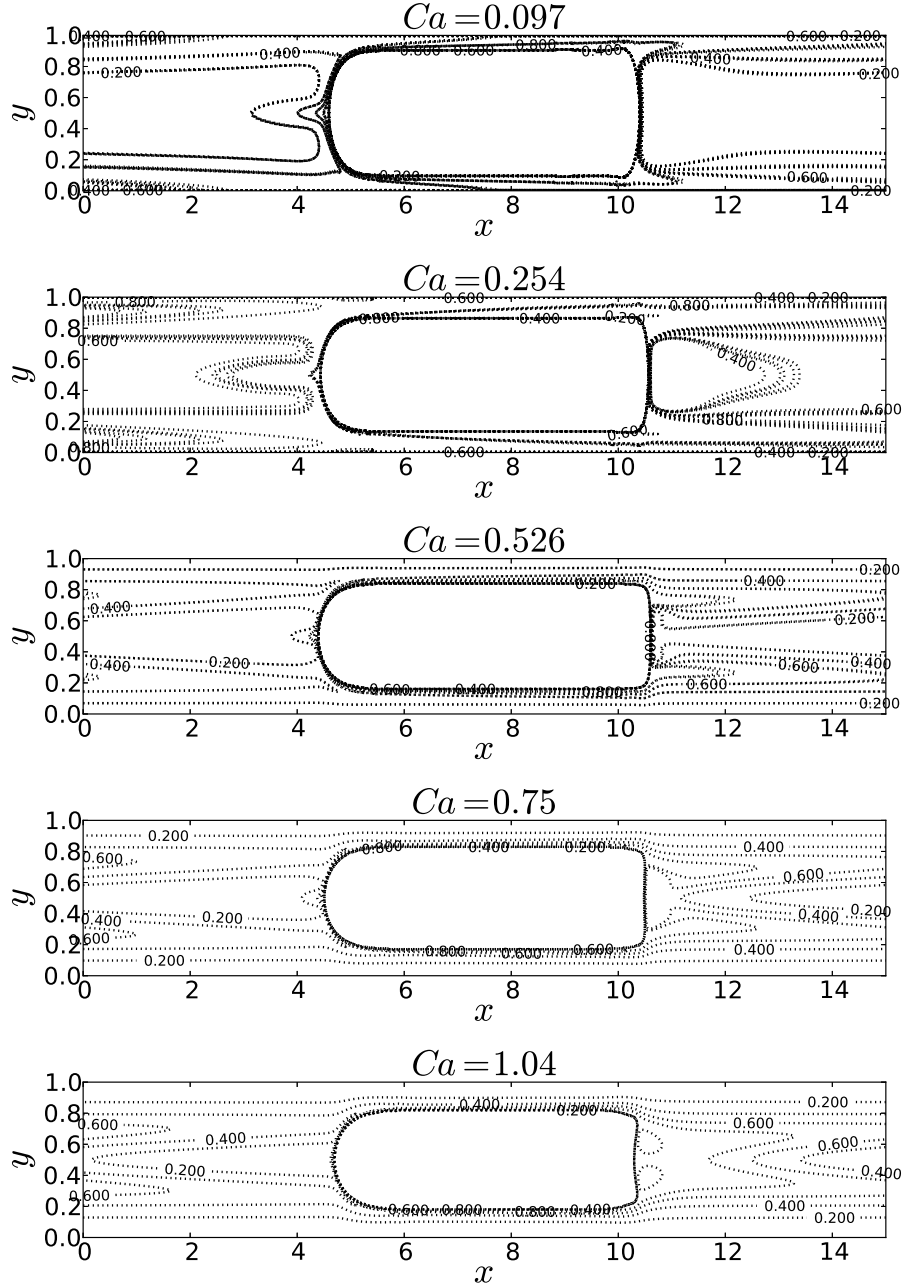


Figure 8: Concentration contour profiles for velocity scalings as identified in Table 2 (top to bottom:  $Ca = 0.097, 0.254, 0.526, 0.750, 1.040$ ). Lines correspond to all different scales indicated in Table 2 (top to bottom: 6 scalings, 5 scalings, 2 scalings, 1 scaling, 1 scaling). Lines for different scaling parameters coincide with or are close to each other showing that simulations with velocity scalings are consistent.

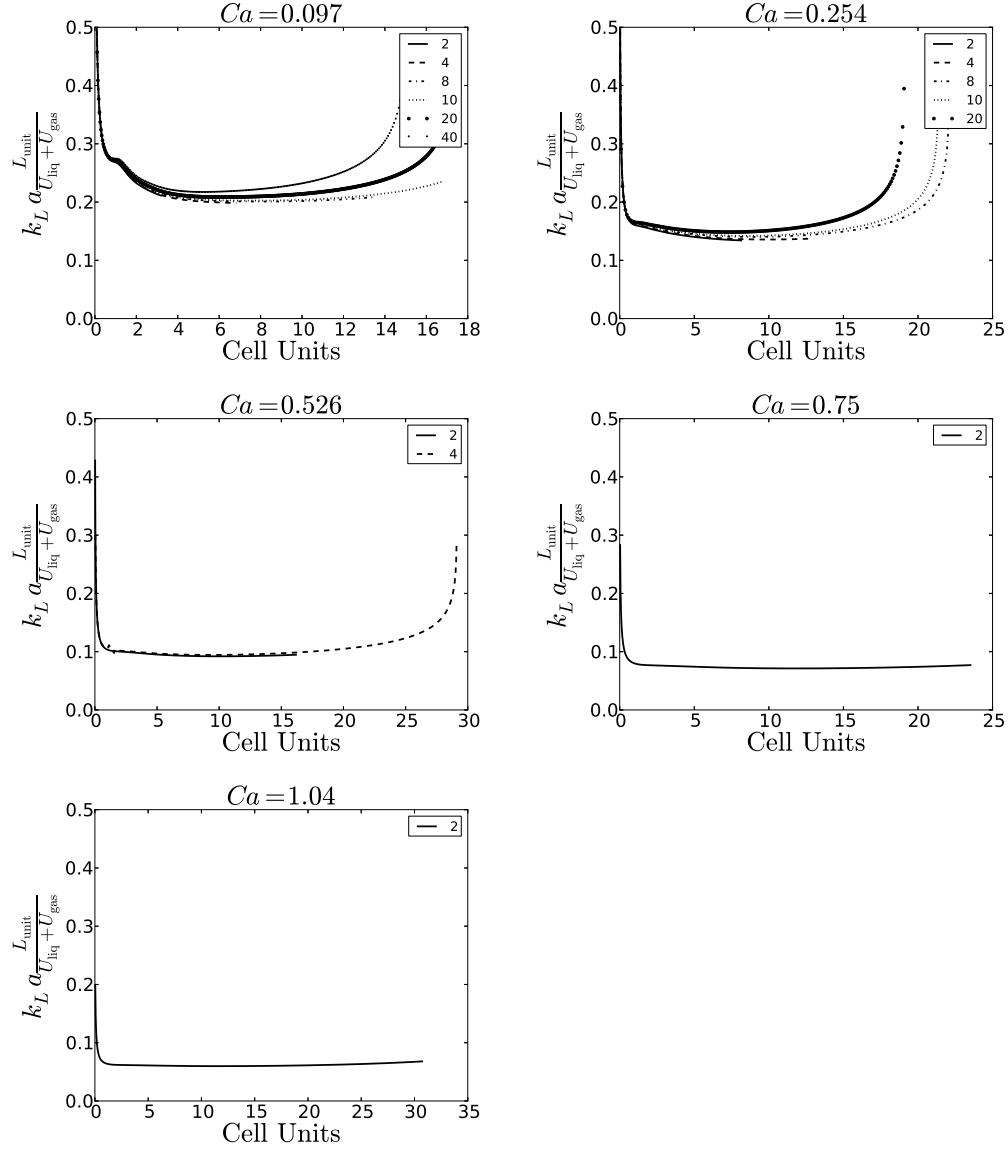


Figure 9: Volumetric mass transfer coefficient for different capillary numbers and velocity scales against the bubble travel distance in the laboratory frame. The "Cell Units" axis refers to the physical distance in unit cells lengths the bubble travels. A legend is provided for velocity scalings. All of them show a good agreement. One can see an abnormal rise of the mass transfer coefficient when the average concentration is close to  $C^*$  due to the logarithmic function evaluation. Table 3 summarizes the results presented here.

$Ca$	$Pe$	$L_{\text{steady}}/L_{\text{unit}}$	$k_L a \frac{L_{\text{unit}}}{U_{\text{liq}} + U_{\text{gas}}}$
0.097	1313	7	0.21
0.254	3414	6	0.14
0.526	7092	3	0.095
0.750	10125	3	0.074
1.040	14041	2	0.0601

Table 3: The distance which a bubble propagates when the steady-state condition is achieved.

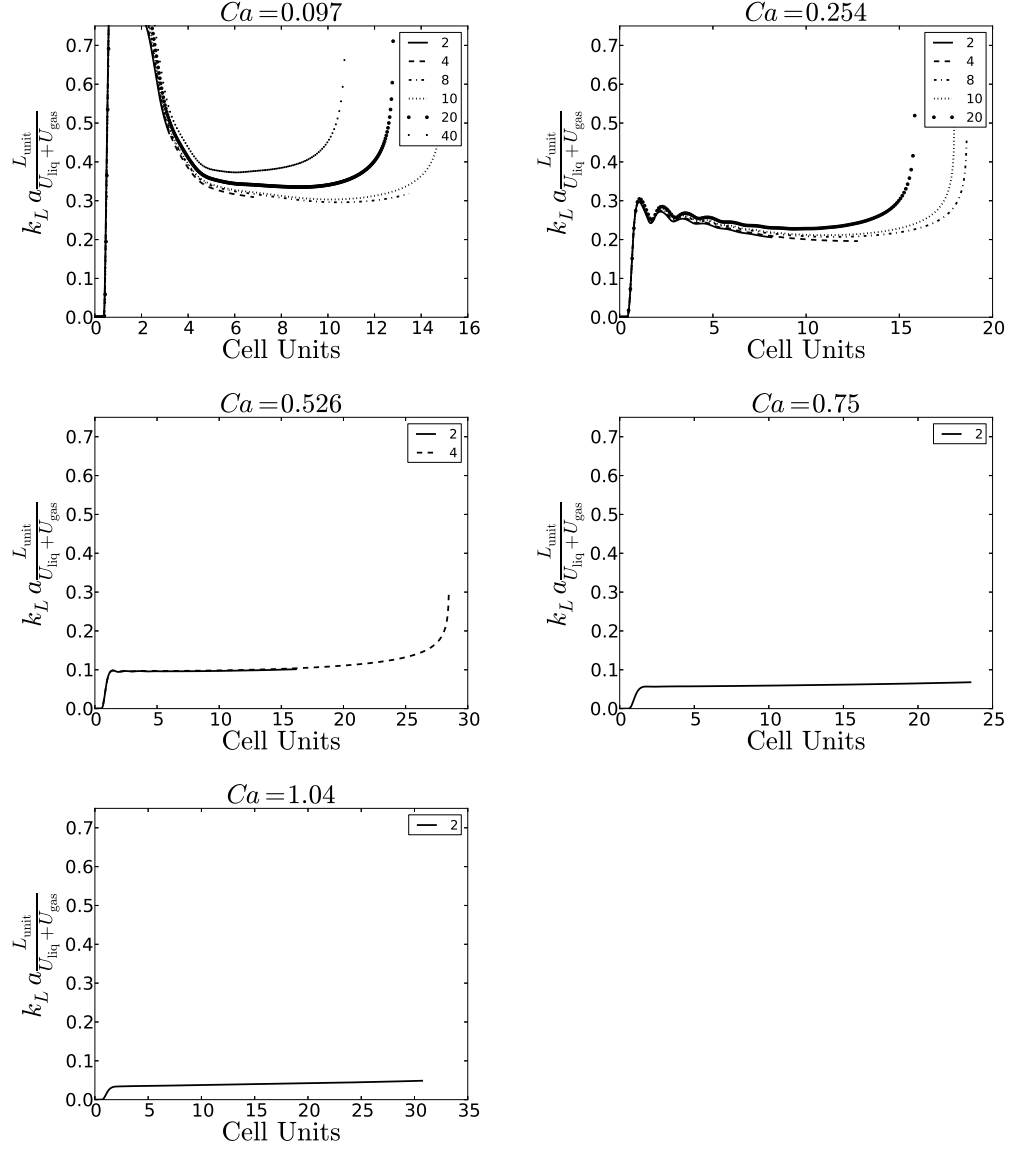


Figure 10: The volumetric mass transfer coefficient with the characteristic concentration based on the inlet/outlet flux averaged concentration as in [2]. One can see that depending on the velocity pattern, the values are either overpredicted or underpredicted in comparison to values specified in Table 3.

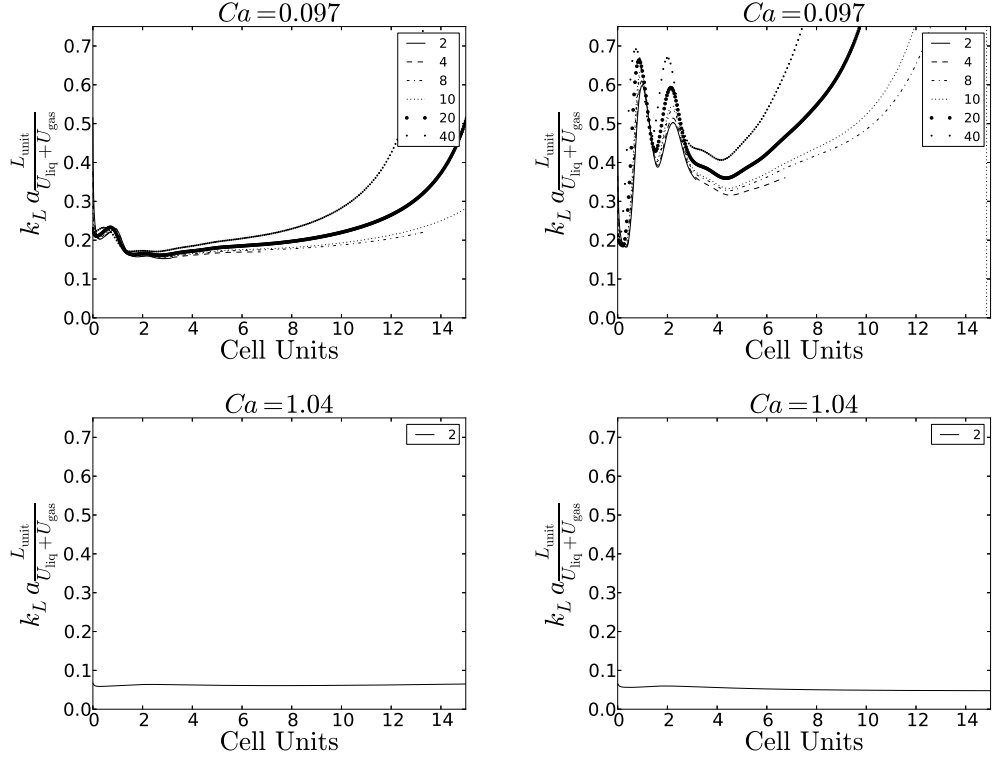


Figure 11: The van Baten and Krishna [2] formulations for  $Ca = 0.097$  (top) and  $Ca = 1.04$  (bottom) with the characteristic concentration being domain-averaged (left) and inlet/outlet flux-averaged (right). One can see that the van Baten and Krishna [2] formulation produces good results with the characteristic concentration being the average concentration. Moreover, the values are closer to values obtained with many cell simulations, see Fig. 12, than with periodic boundary simulations in Section 5.2. The characteristic concentration being inlet/outlet flux-averaged does not produce consistent results.



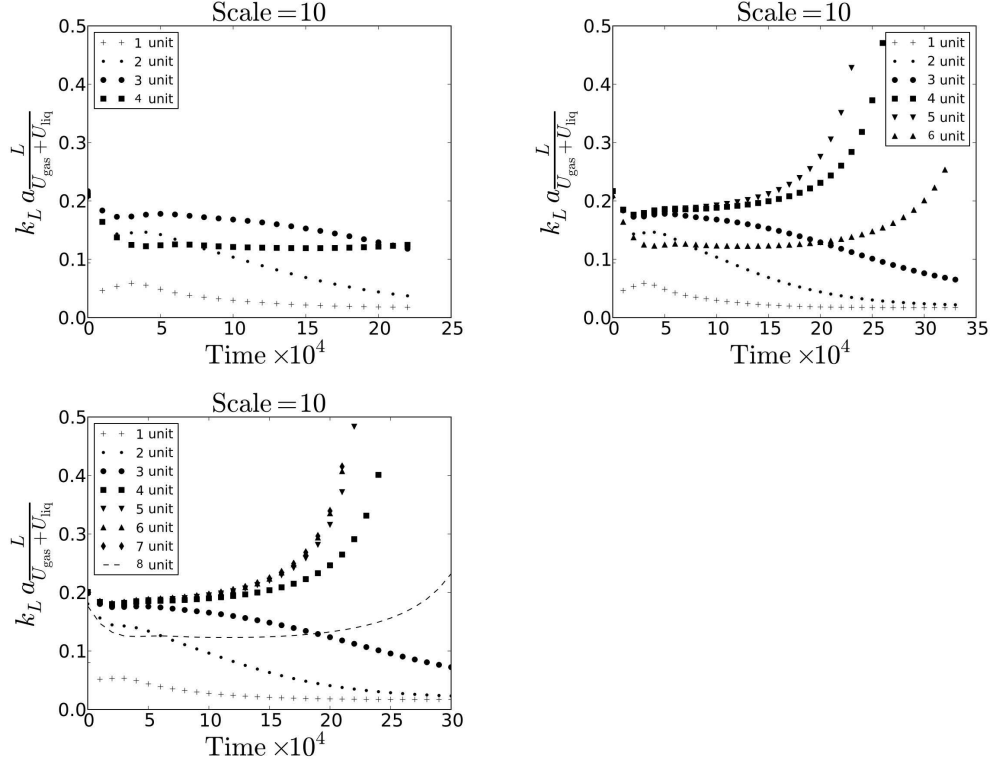


Figure 12: The non-dimensional volumetric mass transfer coefficient defined in Eq. 34 for 4 (top left), 6 (top right), 8 unit cells (bottom). Only scale 10 is presented since all other simulations produce the same results. One can see that 4 unit cells is not enough to avoid the influence of boundaries. However, the results for 6 and 8 unit cells are consistent and show that beginning from the third unit cell and ending with the penultimate cell, the results are consistent with periodic boundary simulations and van Baten and Krishna [2] formulations.

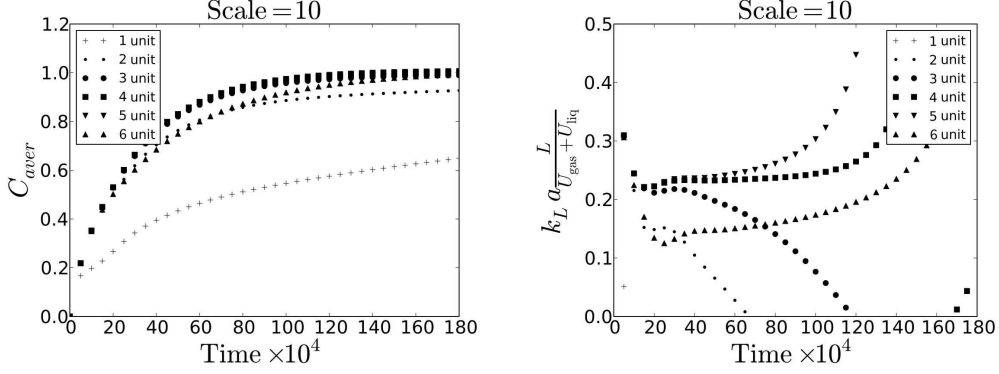


Figure 13: Average concentrations (left) and volumetric coefficients (right) for 6 unit cells. The volumetric mass transfer coefficient is calculated based on Eq. 35 and accounts for inlet and outlet fluxes.

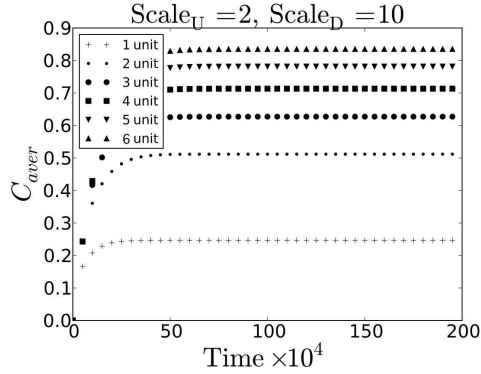


Figure 14: Results for 6 unit cells. The Peclet number is  $Pe = 2644$ . One can see that the average concentrations reach a certain value and stay constant. Thus, the volumetric mass transfer coefficient,  $k_L a \frac{L_{\text{unit}}}{U_{\text{liq}} + U_{\text{gas}}}$ , can be calculated using the spatial approach, see Fig. 15. To decrease the initial Peclet number from 14041 to 2644, the corresponding scaling parameters for velocity and diffusion equal to 2 and 10.

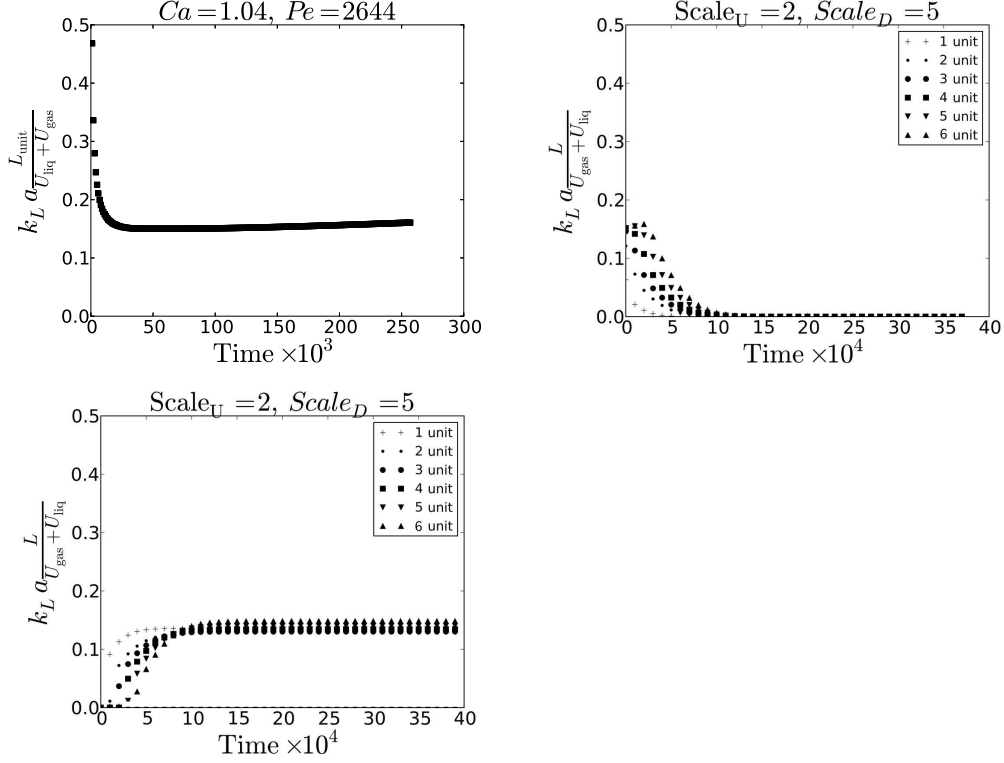


Figure 15: The periodic (top left, 1 unit cell, Eq. 13), unit cells domain-averaged concentrations as a function of time (top right, 6 unit cells, Eq. 13), and spatial location (bottom, 6 unit cells, Eq. 36) calculated volumetric mass transfer coefficients. For the upper right figure, where the time-averaged calculation is presented, one needs to consider only results where there is no concentration saturation. Thus, one needs to consider only results with less than 20,000 iterations as the saturation happens fast due to the high Peclet number. It is not convenient to use them in practical cases for unmixed slugs, i.e.  $Ca > 0.7$ . All results coincide and give value of around 0.15 – 0.16. However, the calculations based on periodic boundary conditions produce a slightly overestimated volumetric mass transfer coefficient.

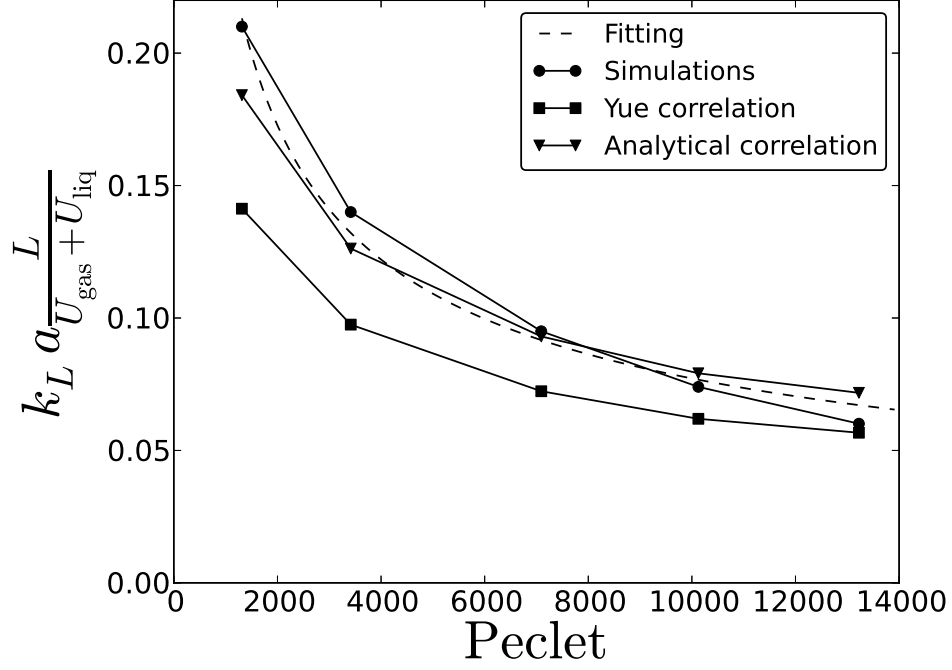


Figure 16: Comparison between the correlation by Yue et al. [7], the analytical correlation derived by following the work [16] and the mass transfer coefficient based on periodic boundary conditions. The fitting curve ( $7.745Pe^{-0.50038}$ ) is proportional to  $Pe^{-0.5}$  which corresponds to all correlations. One can as well see that the deviation from the analytical expression becomes larger with the increasing Peclet number, which happens because the analytical expression does not account for the velocity pattern and the bubble shape change.

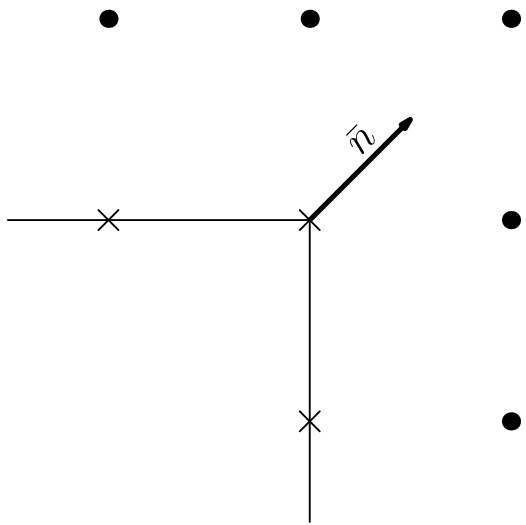


Figure 17: Free-surface boundary condition represented in the lattice Boltzmann method. Boundary nodes are depicted by crosses, and fluid nodes are represented by dots. The populations at the corner boundary nodes are essentially the populations of the fluid node, but in a different order.